Mitigating tsunami effects on buildings via novel use of discrete onshore protection systems

Document Version
Accepted author manuscript

[Link to publication record in Manchester Research Explorer](#)

Citation for published version (APA):
Pringgana, G., Cunningham, L., & Rogers, B. D. (2023). Mitigating tsunami effects on buildings via novel use of discrete onshore protection systems. *Coastal Engineering Journal*, *65*(1), 149-173.
https://doi.org/10.1080/21664250.2023.2170690

Published in:
Coastal Engineering Journal

Citing this paper
Please note that where the full-text provided on Manchester Research Explorer is the Author Accepted Manuscript or Proof version this may differ from the final Published version. If citing, it is advised that you check and use the publisher's definitive version.

OPEN ACCESS

Mitigating tsunami effects on buildings via novel use of discrete onshore protection systems

Gede Pringgana[1], Lee S. Cunningham[2], Benedict D. Rogers[3]

[1]Lecturer in Civil Engineering, Faculty of Engineering, Udayana University, Bukit Jimbaran 80361, Bali, Indonesia. E-mail: gedepringgana@unud.ac.id.

[2]Senior Lecturer in Civil Engineering, Department of Mechanical, Aerospace and Civil Engineering, The University of Manchester, Manchester M13 9PL, UK. E-mail: lee.scott.cunningham@manchester.ac.uk.

[3]Professor, Chair of Computational Hydrodynamics, Department of Mechanical, Aerospace and Civil Engineering, The University of Manchester, Manchester M13 9PL, UK. E-mail: benedict.rogers@manchester.ac.uk.

Corresponding Author: gedepringgana@unud.ac.id

Abstract

This study investigates the effectiveness of a new discrete V-shape coastal barrier (V-wall) to reduce multiple tsunami-bore impacts on a group of idealized coastal structures. The performance comparison has been made between a baseline model (BM), continuous straight wall models (SW) and V-wall (VW) models. A number of key parameters including the barrier height and length along with the arrangement of the landward structures are investigated numerically using the 3-D smoothed particle hydrodynamics (SPH) approach. From the SPH models output the bore velocity, maximum force, total impulse and pressure distribution on the structures are examined. The results indicate that the V-walls can provide a similar level of protection to continuous seawalls of the same height and hence can be considered as an economic alternative to protection in tsunami prone regions. However, in order to gain the greatest benefit from the V-walls, strategic planning of the position and orientation of landward structures and the walls themselves is needed to avoid bore flow focusing and reflection effects.

Keywords: building structures, coast protection, overtopping, SPH, tsunami, wave forces.

1. Introduction

The protection of onshore building infrastructure from tsunami wave impact can be delivered by means of coastal defence structures including barriers, seawalls and embankments (Xu et al. 2021, Syamsidik et al. 2019, Abe et al. 2012). Considering typical tsunami wave characteristics, the cost of traditional coastal defences to provide a measure of protection to shore-based structures can be very considerable and thus prohibitive in many parts of the developing world. Aside from the cost of such defences, a continuous seawall of the height necessary for tsunami protection may in some cases be inefficient, especially in

conditions where the protected buildings are clustered locally e.g. in case of apartment buildings that are located near to the shoreline (Yeh et al. 2013). There is also the aesthetic concern of lost view and amenity whereby a continuous seawall will block beach access and the views which are important aspects for the tourism industry. In Namiita-Japan for example, residents opposed the reconstruction of the seawall entirely to preserve the natural scenery, while in Akahama-Japan, the residents' consensus was to keep the seawall at its previous level and move the residential area to higher ground to preserve the scenic benefits (Burnett et al. 2016). In order to protect buildings located in tsunami prone areas, it is necessary to consider alternative protection systems that can reduce tsunami loads on buildings and improve survivability. The tsunami resilience of building structures has conventionally been achieved by several strategies including the presence of openings or breakaway walls or by elevating the structures (Moon et al. 2020). In parallel with these direct interventions to the buildings themselves, modification of the coastal defence system seaward of these buildings has the potential to reduce tsunami loads and further improve building performances.

Recent studies have examined influential factors on tsunami impact force reduction in regards to an on-shore structure's orientation and position. Shafiei et al. (2016) investigated experimentally the effect of rotation of a single structure changes the pressures and forces it experiences. For the case of flood inundation, Cantelmo and Cuomo (2020) proposed a generic formulation for evaluating dynamic loads on a structure that can be used to assess its vulnerability and also to design new flood-resilient structures. They conducted a series of tests to study the sensitivity of loading to the orientation angle of structures relative to the flow direction and proposed an equation based on best-fit curves with empirical parameters for impulsive and quasi-static loading conditions. Tomiczek et al. (2016) used experiments to examine shielding effects of an array of regularly spaced structures showing that peak

pressures of the breaking waves can be reduced by 30-70%. Pringgana et al. (2021), using a smoothed particle hydrodynamics (SPH) numerical simulation approach, showed that the tsunami load reduction on a building is heavily influenced by its orientation and that of neighbouring structures to the oncoming tsunami wave direction. Moris et al. (2021) studied the influence of a building array on tsunami-driven run-up loads and found that the number of rows of buildings providing shelter is an explanatory variable for the maximum wave run-up load reduction.

Kihara et al. (2021) performed a series of physical model experiments of tsunami inundation over an idealized industrial site located in a coastal area. They found a wide spatial variance of the maximum inundation depth influenced by the effects of the neighbouring structures, especially the blocking effects due to structures. It was also underlined that, for a relatively small inundation area, as the distance increases from the coastline, the contribution of hydrodynamic pressure decreases and the momentum fluxes and Froude numbers do not always agree with those stated in previous studies. Recently, Zhang et al. (2023) have conducted one of the first experimental investigations of the inundation of an idealised urban area behind a partial wall showing the partial wall provides an extended sheltering effect on the structures. Moreover, Fukui et al. (2022) performed a direct simulation of inundated developed urban areas compared to that of bare earth with roughness and stated that buildings significantly influenced the overland flood propagation. The significant effect of buildings on tsunami flow has been studied experimentally and numerically using OpenFOAM by Ishii et al. (2021). They also revealed a considerable shielding effect occurred in the leeside of the building where this condition can be used for constructing safer evacuation strategies.

Although some research has been carried out on a structure's orientation, where the angle of rotation has been found to be related to impact force reduction, no studies have been

3

conducted which examined the implementation of protective structures with oriented surfaces, thus the extent of its wider relevance remains unknown. The aim of the present study is to explore the effectiveness of discrete protective structures, namely on-plan V-shaped walls, in reducing the tsunami wave impact force on building structures and to observe the minimum size of V-wall that can provide a comparable level of protection given by a continuous sea wall.

The efficacy of SPH for modelling the tsunami wave interactions with coastal structures has been developed through various numerical validations using the open-source SPH code DualSPHysics (Domínguez et al. 2021). Pringgana et al. (2016) re-modelled the dam-break case of Kleefsman et al. (2005) to investigate the sensitivity of SPH particle size to several parameters including the water surface elevation and pressure. SPH approaches for investigating tsunami wave and structure interaction utilizing a larger numerical flume size has been conducted by Cunningham et al. (2014), following an experimental investigation conducted by Linton et al. (2013). The numerical and experimental output comparisons showed good correlation in terms of water surface elevation, wave velocity and pressure over the vertical surface of the impacted wall. Cunningham et al. (2014) has also demonstrated the suitability of SPH modelling to predict the tsunami wave force on discrete, non-orthogonal structures in comparison to the corresponding experimental results by Zhang (2009). More recently, Pringgana et al. (2021) confirmed that the SPH numerical modelling using DualSPHysics was capable of predicting the tsunami wave and structure interaction for an array of structures reproducing and extending the experiments conducted in a large wave basin by Thomas et al. (2015).

The current paper is structured as follows. The Methodology section presents a brief description of SPH and is then followed by the Numerical Setup that describes the layout of

numerical boundary models and modelling scenarios. The Results and Discussion provide the outcomes of the numerical work, these are then followed by the Conclusions.

2. Methodology

The numerical technique smoothed particle hydrodynamics (SPH) is an increasingly popular method for simulating coastal engineering applications (Altomare et al. 2015; Domínguez et al. 2021). SPH is a meshless weakly compressible Navier-Stokes solver that is capable of simulating violent free-surface flows including tsunamis. In recent years, the accuracy of SPH to predict physical processes has been improved continuously with hardware acceleration to reduce the computational cost. Based on Domínguez et al. (2021), the SPH formulations consist of several key aspects that can be listed as follows: (1) interpolants and kernel functions, (2) governing equations, (3) SPH discretization of the governing equations, (4) equation of state and compressibility, (5) time integrators and time step, (6) boundary conditions and (7) particle shifting algorithm. Those key aspects are briefly described below.

The properties of the SPH particle are influenced by its neighbouring particle within the kernel. The integral interpolant for approximating the quantity value of an SPH particle $A(r)$ located at position r can be written as follows (Gomez-Gesteira et al. 2012):

$$\langle A(\boldsymbol{r}) \rangle = \int_{\Omega} A(\boldsymbol{r}')\boldsymbol{W}(\boldsymbol{r} - \boldsymbol{r}', h)d\boldsymbol{r}' \tag{1}$$

where $W(\boldsymbol{r} - \boldsymbol{r}', h)$ is the weighting function or smoothing kernel, h is the smoothing length that controls the radius of influence of domain Ω and $\langle ... \rangle$ denotes an approximation. Eq. 1 is discretised using a summation:

$$\langle A(\boldsymbol{r}_a) \rangle = \sum_{b} A_b \boldsymbol{W}_{ab} \frac{m_b}{\rho_b} \tag{2}$$

where $\boldsymbol{r}_a$ is the position of particle a, subscript a refers to the particle of interest, subscript b refers to neighbouring particles, $\boldsymbol{W}_{ab} = \boldsymbol{W}(\boldsymbol{r}_a - \boldsymbol{r}_b, h)$, m is the mass and ρ is density. The

kernel function controls the influence of SPH particles that have mass and density, within the compact support of the smoothing kernel. There are several types of kernels that can be implemented in DualSPHysics including the Cubic Spline, Wendland and Gaussian (Dehnen and Aly 2012). The Wendland kernel was used for all numerical models in the present study. The Navier-Stokes governing equations of continuity and momentum determine the velocity, density and pressure, which also consider the dissipation terms and accelerations due to external force such as gravity. The governing equations are then discretized to be used in SPH by conservation of the mass and momentum Domínguez et al. (2021).

The weakly compressible SPH model solves the conservation of mass and momentum in Lagrangian form as

$$\frac{d\rho}{dt} = -\rho \nabla \cdot \boldsymbol{v} \tag{3}$$

$$\frac{d\boldsymbol{v}}{dt} = -\frac{1}{\rho}\nabla P + \boldsymbol{g} + \boldsymbol{\varGamma} \tag{4}$$

where $\boldsymbol{v}$ is the velocity, t is the time, ρ is the density, P is the pressure, $\boldsymbol{g}$ is the gravitational acceleration and $\boldsymbol{\varGamma}$ is the dissipative term. In SPH form, the continuity equation, Eq.3, can be written using the δ-SPH formulation (Antuono et al. 2015):

$$\frac{d\rho_a}{dt} = \sum_b \boldsymbol{v}_{ab} \cdot \nabla_a \boldsymbol{W}_{ab} \frac{m_b}{\rho_b} + \delta^{SPH} \tag{5}$$

where $\boldsymbol{v}_{ab} = \boldsymbol{v}_a - \boldsymbol{v}_b$ and $\nabla_a \boldsymbol{W}_{ab}$ denotes the derivative of the smoothing kernel $\boldsymbol{W}_{ab}$ with respect to the coordinates of particle a. The conservation of momentum as shown by Eq. 4, can be expressed in the SPH notation related to pressure gradient as follows:

$$\frac{dv_a}{dt} = -\sum_b m_b \left(\frac{P_a + P_b}{\rho_a \rho_b} + \Pi_{ab}\right) \cdot \nabla_a \boldsymbol{W}_{ab} + \boldsymbol{g} \tag{6}$$

where Π_{ab} represents viscous forces.

Recently, stability improvement in DualSPHysics has been performed by implementing the density diffusion term (DDT) formulations that smooth the density and

6

pressure so that high frequency noise can be filtered (Fourtakas et al. 2019). The density and pressure in SPH are formulated by an equation of state that allows for weak compressibility of the fluid and incorporates the speed of sound parameter. The time integrator regulates calculation steps within an iteration time interval. The Symplectic time integration scheme available in DualSPHysics with variable time stepping was used in this study where it is time reversible and symmetric in the absence of diffusive terms.

Periodic lateral boundary conditions are used to simulate an infinitely long domain is applied in all numerical models in this study, while the dynamic boundary condition has been used for all solid boundaries (Domínguez et al. 2021). The DualSPHysics software possess specific functionality for wave generation including regular, random and solitary waves. The solitary waves, as used in all models in this study, are generated by the displacement of a piston-type wavemaker where its motions are based on the Boussinesq approach (Goring, 1978).

Generally, the SPH pressure distribution over a surface of a structure is measured by numerical probes. Pressures measured on a surface can be multiplied by the area of structure's surface to obtain force, as described in Pringgana et al. (2021). The inter-particle spacing of a group of measuring pressure probes and their distances from the surface of structures are sensitive to the resulting numerical prediction so that prior sensitivity studies are required to achieve numerical pressure predictions comparable to the experimental data. However, recent progress in DualSPHysics 5.0 provides the users a straightforward means to measure force on a surface of a structure, using the ComputeForce calculation tools. The ComputeForce tool enables the measurement of force on the surface of the boundary, the surfaces are set during the pre-processing stage and the results can be directly found in the post processing output files. The ComputeForce tool has a similar function to the force measurement tool by using measuring probes placed on the front of certain surfaces. The use

of measuring probes to determine force can be found in Cunningham et al. (2014), Pringgana et al. (2016) and Pringgana et al. (2021). Other functionality available in DualSPHysics 5.0 is the FlowTool that can be used to calculate the number of fluid particles that enters or leaves a certain domain specified by the users.

3. Numerical set-up

The numerical domain consists of water particles, a continuous straight wall (SW) as a protecting barrier, an inverted V-shape wall (herein referred to as a V-wall, VW) and cuboid structures representing buildings (S), as shown in Figure 1. The principle behind the use of such discrete structures is to develop a cost-effective alternative to continuous sea walls. In addition to construction of dedicated V-shaped wall defences, such an approach may also allow the external walls of strategically placed existing and new structures to be strengthened to act in a similar way to V-wall defences. Intuitively, when considering purely the structural action of the walls, it would be expected that the structural demand on the V-walls would be less when the V-shape is orientated offshore i.e. apex pointing towards the oncoming flow, compared to the reverse orientation. Similarly, the offshore V-orientation lends itself better to incorporation in building structures compared to the reverse situation. Consequently, the work herein focuses on the offshore V-shape orientation. However, for interest, the reverse orientation of the V-shape has also been examined, the results from this are given in appendix A.

Numerical models in this study are classified into several groups which depend on the types of coastal defence structures involved together with a baseline model (BM) without any coastal defence barrier. All models consist of 11 cube structures placed in three rows (S11 – S34), except model VWX which consists of 10 cubes since the central structure, S22, is excluded. The domain is dimensioned in terms of the characteristic length of a structure D.

The first group consists of two models similar to the baseline model but incorporating a continuous straight wall (SW1 and SW2) with different heights (0.15 m and 0.30 m), as illustrated by Figure 1(a). The second group comprises models similar to the baseline but with V-walls varying in size and height (VW1-VW6), as can be seen in Figure 1(b). The third group contains models similar to the second group but with modification on the central cube structure (S22), whereby S22 is rotated in models VWR1, VWR2 and VWR3, and S22 is excluded in model VWX. Table 1 summarizes the details of all models. In this study, all spatial dimensions are set to be the multiple of D for convenience, where D is the size of the cube structure.

The SPH periodic boundary condition was utilized to numerically represent an infinitely long coastline using a finite domain with a length of $16D$. The straight continuous walls (SW) and discrete V-walls (VW) have the same thickness of $D/3$ (0.2 m). The V-walls, as shown in Figure 1(b), vary in length from $L = 2D$, $3D$ and $4D$. The position of SW, as well as the $2D$-length VW in the x-direction, were set in such a way that the centroid of both SW and VW is located at the same point, where the centroid lies between the shoreline and the most seaward structure. In this study, two heights of the protective walls VW were considered, namely $D/4$ (0.15 m) and $D/2$ (0.30 m). The variation of VW size was intended to study the effect of VW's length and height on the resulting total force on structures. The shape of VW and its orientation was arranged so that both of its sides formed a 45-degree angle with regard to the shoreline and oncoming tsunami waves. The configurations defined here are based on findings by Pringgana et al. (2021) that revealed the 45-degree rotation of rectangular structures provides the most significant total force reduction from tsunami wave impact as compared to other degrees of rotations (e.g. 15, 30, 60-degrees).

The tsunami-like wave simulation in all models involved two solitary waves that were generated sequentially by piston wave-maker motions, with an interval period of 1 second,

which was based on the Boussinesq equations (Goring 1978). This interval period allowed the second solitary wave to be produced with the same number of particles in the computational domain (e.g. the height of water particle in front of paddle wavemaker) following the generation of the first wave. Note, after the generation of the first wave, the paddle remains stationary until the paddle restarts moving for the generation of the second wave. Both solitary waves were propagated from offshore to the flat onshore side where the structures are located, as illustrated in Figure 2. The reason for applying multiple solitary waves in this model was based on the fact that tsunamis consist of a series of waves. The use of solitary waves to approximate tsunami waves has become customary due to their stable form, experimental repeatability along with the fact that the leading wave of tsunamis often emerges as a solitary wave after a long period of propagation (Yeh et al. 1994). However, Madsen et al. (2008) criticized the use of solitary waves for modelling tsunami waves due to their differences in wavelength and period. The first tsunami might not be the strongest and the second wave could get bigger. In this study, both solitary wave heights were set similar to that of the cube structure's height, D (0,6 m).

SPH particles were used to create the boundaries in the models, including the fixed, periodic and moving boundaries as well as the fluid particles. The fixed boundary comprises the water tank and all structures, and the moving boundary is used for the piston wave-maker. Based on previous particle convergence studies by Pringgana et al. (2021), who identified that a suitable particle size is $D/10$, using the same basic flume dimensions and wave characteristics, the SPH particle size used in all models is $d_p = 0.025$ m to represent bore flows. The SPH modelling output examined in this study includes the wave height, wave velocity, wave pressure, impact force, impulse and momentum flux. The numerical velocity probes (P1-P4) for measuring the velocity and also the height of fluids were located at offshore and onshore zones inside the water tank for all the models described in Figure 1. The

positions of the water surface elevation and the offshore velocity probes denoted as WG1-WG4, are shown in Figure 2. The vertical surfaces of the cube are set-up to automatically measure any resulting hydrodynamic force.

4. Results and Discussion

4.1 Pre- and Post-processing Data of SPH Modelling

The numerical modeling constants and parameters in DualSPHysics 5.0 are shown in Table 2. The SPH simulations were analyzed using commercial GPU hardware, Nvidia GeForce GTX 3060, which has 12,288 MB of memory and 1.85 GHz clock rate. The computational time of the simulations and the number of particles involved, based on diameter of SPH particle d_p = 0.025 m, are listed in Table 3 for selected cases. The SPH particles comprised the fixed boundary (water tank, idealized structures, numerical measuring probes), moving boundary (paddle wave-maker), and fluids (water in the tank). Note that the number of particles for moving boundary and fluid particles are the same for all models. An open-source visualization application named ParaView was used to analyze SPH output data to produce the 2-D and 3-D figures in this study.

4.2 3-D Flow Simulations

Figure 3 depicts the numerical simulation of the model without any protection wall, i.e., the baseline model (BM). The 3-D side view in Figure 3(a) shows the paddle wavemaker displacement generated by two solitary waves propagating toward the onshore side. As the solitary waves reached the shoreline, they each formed a bore and impacted the group of onshore structures, as shown by the seaward view in Figure 3(b). The second bore impact on the structures is shown by the landward view in Figure 3(c). Figure 4 shows the landward and seaward views for the case with a straight wall (SW2), capturing the phenomenon of the first wave impact at the wall, the overtopping and the second wave offshore plunging. During the

wave overtopping, some fluid particles were observed to either move forward or bounce back offshore. By using the straight wall as a reference line for dividing the shore and the built-up areas, the number of fluid particles that either moved forward or bounced back can be calculated using the FlowTool in DualSPHysics. In Case SW1 and SW2 (with 0.15 m and 0.30 m wall heights), the total volume of fluid particles per unit length (m) that overtopped the straight walls and entered the built-up areas were 1.121 m^3/m and 0.525 m^3/m, respectively.

The simulation of case with V-walls (VW5) is depicted by the landward view in Figure 5. It can be seen that the 0.30 m-high V-walls provided shielding to the rear structures and at the same time incurred focusing of flow to the centre structure S22. When compared with the straight wall (SW2) of the same height as shown in Figure 4(c), the V-walls of VW5 can provide a better level of protection to the structures from bore impact.

4.3 Water Surface Elevation and Velocity

The offshore heights of two solitary waves in Figure 3(a) were comparable and stayed stable throughout offshore propagation and then increase while passing over the sloping bed and moving closer to the shoreline, as shown by Figure 6(a). The offshore velocities of both solitary waves show the same trend as that of their offshore heights. However, the offshore velocity of the first solitary wave seems considerably higher than the second one as it is closer to the shoreline, as shown by Figure 6(b). Moreover, offshore velocity probes recorded negative velocity with increasing value closer to the shoreline, which indicates a certain number of fluid particles moved offshore.

The onshore bore maximum velocities that were measured by numerical probes P1-P3 are plotted in Figure 7. The bore velocities at the shoreline for Case 1 (baseline) is represented by line P1-C1 in Figure 7(a). Furthermore, the bore maximum velocity increased

as the bore proceeded further towards the structures, as shown by line P2-C1 and P3-C1. The maximum velocities were influenced by the changing shape of the wave, where the wave broke near the shoreline and then travelled as a bore on the onshore flat surface. This explained the fact that the maximum velocity at P1-C1 is lower than that of at P2-C1 and P3-C1. The bore velocity decreased as the height of the straight wall increased, as shown in Figure 7(b) which compares the bore velocities of baseline case, SW1 and SW2 at probes P3 located just before the first row of structures.

The shape of V-wall triggered the focusing flow toward the structures as depicted by Figure 5. The velocity of associated focusing flows measured by probes P3 (see Figure 1b) and plotted in Figure 7(c). Based on Figure 7(c), it can be observed that the influence of the V-walls' height and width were not significant to the flow velocities during the first bore impact and less significant during the second bore impact.

The bore velocities at probe P4 which is located behind the V-wall are shown in Figure 8. By comparing the baseline, BM, and straight wall cases, SW1 and SW2, through Figure 8(a), it can be observed that the bore velocity at P4 is reduced by the presence of the straight walls. However, related to the first bore strike, the higher straight wall (series P4-C3) resulted in a higher velocity than the lower one (line P4-C2), this may be due to the higher overtopping height associated with the higher wall seen in Figure 9(a and b), which was then followed by stronger downfall compared to that of the lower straight wall case. Figure 8(b and c) show that the V-walls (line P4-C4 and P4-C7) eliminate the first wave and were slightly more effective in reducing the bore velocity as compared to the straight walls of the same height (line P4-C2 and P4-C3). Figure 9(c, d) and Figure 9(e, f) show the overtopping waves on the straight and V-walls, respectively, due to the second bore strike.

4.4 Bore Impact Force

The bore impact force is represented by Figure 10 and Figure 11 showing the comparison of applied force on structures in the baseline model (BM), the straight wall (SW) and the V-wall (VW) models of the same height. The position of graphs in Figure 10 and Figure 11 was arranged to be similar with the position of structures in the water tank whereby the first row is the closest to shoreline. The impact force data were shown from 8 seconds to 16 seconds, disregarding prior zero impact force data during the time span of offshore to onshore wave propagations. The force lines in the graphs consist of two peaks that represent the influence of the first and second bore strikes. In Figure 10 and Figure 11, it can be seen that the peak impact force values caused by the first bore strike are generally lower than that caused by the second bore strike. In some cases (C8, C9, C11, C12, C13), the first impact is entirely avoided corresponding to the flow visualized in Figure 5. Moreover, the graphs show that the impact force values on structures at the second row are higher than that in the first row, especially for the centre structure, S22. The impact force tends to decrease on the third-row structures. Whilst the graphs provide visual information regarding the impact force comparison, Table 4 through Table 6 provide the maximum impact force values and the total impulse on the structures. The maximum impact force has considered the direction of force acting on each side of the structures, following the approach detailed in Pringgana et al. (2021).

4.4.1 Maximum Bore Impact Force

The maximum impact forces on structures of each case are shown in Table 4. The fluctuations of maximum impact force values on structures were influenced by the dynamic motion of fluid particles of the leading bore. For example, based on data in column 3 of Table 4 for the baseline model (BM), the coefficient of variation (COV) of impact force values on the first, second and third-row structures are 11.3%, 8.6% and 26.3% due to the first bore strike and 5.6%, 14.4% and 6.7% due to the second bore strike. The same trend for force

fluctuations occurred for the rest of data in Table 4, thus, for convenience, the mean values of impact force on structures per row will be used for onward comparison. Based on data in Table 4, the percentage of the mean values of impact force on structures between each model over the baseline model (BM) are determined and displayed in Table 5. The positive values in Table 5 indicate the amount of force reduction provided by the combination of barriers and structures and conversely, the negative values implied force amplification.

In column 3 of Table 4 for BM, the mean values of maximum impact force on the first, second and third-row structures due to the second bore strike are 21%, 58% and 327% higher to that of caused by the first bore strike, owing to the contribution of the wet bed condition following the first bore onshore propagation. The increase of the mean value of maximum impact force on the second and third-row structures was also caused by the flow focusing effect triggered by the interaction of fluid flow with adjacent front structures. A substantial force increase on the third-row structures was caused by the significant number of water particles that were reflected by the second-row structures, as depicted in Figure 13(a). The maximum impact force in cases with the straight wall, SW1 and SW2, are shown in column 4 and 8 of Table 4. It can be seen that the presence of the straight wall was capable of reducing the maximum impact force on structures at the first, second and third rows due to the first and second bore strikes.

From Table 4, there is a clear effect of the V-walls in reducing the impact force, particularly on structure S21 and S23 that were situated precisely behind the V-wall. The wider the V-wall, the more effective the level of protection offered compared to the traditional straight wall, as can be observed from column 10 through 15 of Table 4. However, the V-walls exhibited some drawbacks, mainly to the middle structure S22, in the form of reflected bore flows caused by the inward-inclined shape of the V-walls. From column 5

through 7 and column 9 through 11 in Table 4, the maximum forces exerted on S22 are significantly higher than that of the baseline and the straight wall.

A means to overcome this drawback is the rotation of structure S22 by 45 degrees along its vertical axis. This rotation yielded lower maximum forces on S22 as can be seen in column 12 through 14 of Table 4. The force on the rotated structure S22 is then compared with an empirical prediction proposed by Cantelmo and Cuomo (2020) that specifically addressed building orientation under either impulsive or quasi-static loadings. The best-fit curves of the impulsive loading in Cantelmo and Cuomo (2020) re-produced as a dashed line in Figure 12 relates the normalized force on the rotated structure $F(\theta)$ over that in the un-rotated structure $F(0)$ and the degree of the structure's orientation $(\theta-0)°$. Based on the data in column 9 through 14 of Table 4 for models VWR1, VWR2 and VWR3 under the first and second bore impact, the SPH maximum impact force predictions are plotted against the empirical maximum force prediction. It can be seen from Figure 12 that the SPH prediction due to the first bore strike (black) are close to the empirical prediction. However, the SPH prediction due to the second bore strike (grey) are in the case of VWR1 and VWR3 up to +/-30% different, this may be influenced by different hydrodynamic conditions. The empirical prediction was based on a single load on a single structure, while the second SPH bore strike may be affected by earlier bore-structure interactions.

A further shortcoming arose from the rotation of S22, also in the form of reflected bore flows to nearby structures, mainly third-row structures, S32 and S33, as depicted by Figure 14(a, b) and also indicated by the increase of force in column 12 through 14 of Table 4. To avoid the reflected bore flows, the exclusion of structure S22 was considered as simulated by Figure 14(c), where this consideration resulted in lower maximum force on structures as shown in Table 4 by column 15 versus column 11 and 14.

Based on data in column 3 of Table 5, the maximum impact force reduction provided by straight walls in SW1 on the first, second and third-row structures are 51%, 51% and 11% due to the first bore strike and 19%, 38% and 29% due to the second bore strike, respectively. Moreover, in column 7 of Table 5, the maximum impact force reduction provided by straight walls in SW2 on the first, second and third-row structures are 67%, 57% and 76% due to the first bore strike and 56%, 55% and 62% due to the second bore strike, respectively. These results clearly indicated that a higher straight wall gave higher level of protection.

The effectiveness of the 0.15 m-high straight wall (SW1) and V-walls (VW1, VW2 and VW3) can be seen in column 3 through 6 of Table 5. The data shows that VW2 and VW3 are more effective than SW1 only for structures at the first row with maximum force reduction 58% and 69%, respectively. For other rows, the VW1, VW2 and VW3 are less effective than SW1. Due to the first bore strike, VW1, VW2 and VW3 show disadvantages for the third-row structures with force amplification 34%, 78% and 94%, respectively.

Similar trends to the 0.15 m high barrier cases, are also exhibited by the 0.30 m-high straight wall (SW2) and V-walls (VW4, VW5 and VW6) in column 7 through 10 of Table 5. The VW5 and VW6 arrangements show their effectiveness over SW2 for structures at the first row with maximum force reduction 80% and 87%, respectively. Moreover, VW6 gave greater protection than SW2 except for the third-row structures. Due to the first bore impact, VW4, VW5 and VW6 offered a drawback for the third-row structures with force amplification 51%, 115% and 146%, respectively.

The force prediction of models with rotated middle structure, S22 (WR1, WR2, and WR3) over the baseline scenario are shown in column 11 through 13 of Table 5. The rotation of S22 provided a positive effect with force reductions of 57%, 70% and 77% due to the first bore strike and 46%, 60% and 68% due to the second bore strike. The numerical model with

structure S22 excluded to reduce force exerted on nearby structures, provided results as expected, as shown by data in column 14 of Table 5.

The negative values at the third-row structures in Table 5, which were indicated as force amplification, all belonged to the cases with V-walls. Interestingly, those negative values only occurred during the first bore strike, in contrast to that due to the second bore strike. This finding can be related to Figure 13(c) and Figure 14, where the force amplification on the third-row structures influenced by fluid flows that were reflected to the surroundings by the combination of the inclined shape of V-walls and the middle structure S22. Even after structure S22 was excluded, the force amplifications still remained albeit with less magnitude.

4.4.2 Total Impulse

Table 6 shows the total impulse exerted on structures based on a 16 second simulation time for each. The values of total impulse are representing the area under the curves in Figure 10 and Figure 11. The total impulse is considered as a critical parameter in the design of building structures, together with the maximum impact force. In column 3 of Table 6 the presence of traditional straight walls in SW1 and SW2, that are associated with data in column 4 and 8 of Table 6, show significant reduction in total impulse, with mean values ranging from 43% to 49% for SW1 and 80% to 81% for SW2.

The total impulse of 0.15 m-high V-walls are presented in column 5 through 7 of Table 6. The data provides total impulse reduction with mean values up to 29%, 40% and 49% for VW1, VW2 and VW3, respectively. These results indicated that the effectiveness of 0.15 m-high V-walls was generally lower than straight walls in terms of total impulse. The effectiveness of traditional straight wall, SW1, can only be resembled by V-wall, VW3, but limited to structures at the first row, with 49% reduction in total impulse.

The total impulse of 0.30 m-high V-walls are listed in column 9 through 11 of Table 6. The data provide total impulse reduction with mean values up to 36%, 50% and 74% for VW4, VW5 and VW6, respectively. Similar to previous results, the level of protection given by 0.3 m-high V-walls are lesser than the traditional straight wall, SW2, nevertheless, the V-walls still provide substantial reduction in impulse in most locations compared to the baseline scenario.

The numerical models with rotated structure S22, including VWR1, VWR2 and VWR3, provided less significant reduction in total impulse exerted on structure S22, with mean values ranging from 2% to 4%. These results revealed that based on numerical modelling scenarios in this study, the rotation of structures S22 was only significant in reducing the maximum impact force but not the total impulse. Moreover, the rotation of structure S22 deflected bore flows toward structures at the third-row and caused the increment of total impulse for S31-S34 with mean values ranging from 7% to 12%. While removal of structure S22 in case VWX, as predicted, the resulted in the reduction of total impulse for S31-S34 with mean values up to 36%.

4.5 Flow Vector Plots

To further understand the behaviour of the bore flows around the impacted structures, on-plan vector plots are shown in Figure 13 and Figure 14. Figure 13(a) shows the moment the first bore flows interact with the structures, the following second bore flow can be distinguished by the larger arrows offshore. Figure 13(b) displays the case of the straight wall on first bore flow impact on the landward structures and the following second bore flow with some reflection occurring after bore impact on the straight wall as portrayed by smaller arrows. This model shows bore flows with less intensity as compared to the baseline model since the bore energy has been reduced by the straight wall. Figure 13(c) depicts the case of

the V-walls, with a substantial number of fluids being reflected and associated flow focusing towards the rear structures. As a consequence, the flow focusing bore impacted the middle structure and then reflected again to nearby structures, mainly at the rear.

Figure 14 illustrates three simulations, each at the same simulations time of 10.6 seconds, including the 0.30 m-high V-walls and rotated middle structure, S22. Figure 14(a) and Figure 14(b) compare the effect of V-wall length on the flow and reveal reduction in flow velocity and reflections around the structures in the case of the longer wall. Figure 14(c) shows the simulation without S22, here the reduction in fluid velocity and reflections around the adjacent middle row structures and outer third row structures are apparent.

4.6 Pressure Distributions

The numerical modelling in this study provided more specific details about the bore flow interactions with structures, including the pressure distributions on the impacted surface of the structures. Figure 15 shows the seaward views of the baseline model at the time of the first bore impact ($t = 8.9$ seconds) and the following bore inundation ($t = 12.2$ seconds). In Figure 15, it can be seen that the body of structure S12, S13, S22, S32 and S33 are for clarity, depicted as a wireframe and completely transparent, while the rest of structures were maintained as solid. This transparency enabled the observation of fluid pressure distribution over the vertical surfaces of structures. The pressure distribution benefits the building designer in recognizing the most critical part of structures under tsunami bore impact and this pressure information can be related to the force-time history as shown in Figure 10 and Figure 11.

5. Conclusions

This study has numerically investigated the efficacy of a novel V-shape coastal barrier (V-wall) to protect coastal structures from tsunami-like bore impact, as part of strategy for

more resilient coastal communities. The V-walls have shown to effectively reduce the maximum impact force and total impulse on structures especially those located at the front-most (i.e. most seaward facing) row behind the V-walls. For many of the cases examined here, the level of protection offered by the V-walls was similar to that from a continuous straight seawall of the same height. From the particular building arrays examined in this study, the position and orientation of structures needs to be arranged to achieve optimum levels of protection from the V-walls and avoid unnecessary drawbacks caused by flow focusing and reflection. The evaluation for optimum layout and dimension of coastal structures and barriers can be achieved in reasonable time and cost by utilizing numerical modelling software and technique that also capable of exploring essential aspects in engineering practices include the total impulse and pressure distributions. Whilst the V-walls could provide similar degrees of protection to the continuous seawall, the V-walls are built as discrete stand-alone walls and therefore may offer a cost-effective alternative to traditional continuous seawalls. Similarly, the V-walls could be incorporated into seaward facing buildings themselves, whereby the building is oriented 45° to the shore and the seaward façade of the structure is especially designed to resist the associated forces from tsunami impact. Whilst the work undertaken in this study demonstrates the potential of the discrete V-wall concept, the study is limited by the specific wave conditions, bathymetry and onshore spatial arrangements examined. Further investigation is required to understand the influence of variation on these parameters on the relative performance of the V-walls.

Acknowledgments

Appendix A

This appendix details the comparison between the standard V-wall and reverse orientated V-wall in terms of the bore flow pattern and maximum impact forces on the V-wall barriers and landward structures. The V-wall denoted as C8 in Table 1 is examined and its performance in the standard position and in the reverse position is compared. Figure A1(a) to Figure A1(d) depict the bore flows around the barriers and structures. Figure A1(a) shows that during the first bore strike, the area behind the V-wall was well protected without disturbance from the bore flows. In contrast, the reverse V-wall was unable to protect area behind it from the bore impact as shown by Figure A1(b). During the second bore strike, the oncoming bore overtopped all barriers with flow patterns as depicted in Figure A1(c) and A1(d).

Figure A2(a) and (b) show the pressure distribution on the seaward surfaces of the standard V-wall and reverse V-wall during the first bore strike. The standard V-wall split the oncoming bore and the pressure on the V-wall appears to be more evenly distributed along its length, as illustrated by Figure A2(a). The reverse V-wall trapped much of the oncoming bore leading to overtopping and inundation of the area immediately landward. The funneling of the bore flow results in the significant pressure concentration in the central zone of the reverse V-wall as shown in Figure A2(b).

The numerical total force in the x-direction, which was the summation of forces on the two legs of the V-wall barriers, are plotted in Figure A3. As illustrated by Figure A3, the total peak forces exerted on the V-wall were 4232 N and 5252 N during the first and second bore strikes, respectively. Moreover, the total forces applied on the reverse V-walls were 5935 N and 2701 N during the first and second bore strikes, respectively. Figure A4 shows force in the y-direction exerted on each side of the standard V-wall and reverse V-wall. The forces on the standard V-wall in the y-direction are generally higher than that of the reverse V-wall. In a real situation, for the reverse V-wall, the pressure concentrations at the mid-zone and the opposing forces in the y-direction could potentially force the walls apart. Based on this, it could be inferred that the reverse V-walls would need to be of more substantial construction than the equivalent height standard V-wall, this in turn translates to an increased cost.

The maximum force was also measured on the landward structures and is illustrated by Figure A5. The force is examined on the vertical surface of each structure in the x-

direction. Generally, the structures in the first-row experienced greater impact force in the model with the reverse V-wall, where structures S11 and S14 show significant difference during the first bore impact. The effective protection provided by the V-walls is clearly shown for structures S21 and S23 during the first bore strike and also in the contribution to lowering the impact force during the second bore strike. As expected, the maximum impact forces during the first and the second bore strikes on S22 were higher in the model with the V-wall due to the flow focusing effect in the vicinity of S22

References

Abe, T., Goto, K., and Sugawara, D. (2012). "Relationship between the maximum extent of tsunami sand and the inundation limit of the 2011 Tohoku-oki tsunami on the Sendai Plain, Japan." *Sedimentary Geology*, Elsevier B.V., 282, 142–150, https://doi.org/10.1016/j.sedgeo.2012.05.004.

Altomare, C., Crespo, A. J. C., Domínguez, J. M., Gómez-Gesteira, M., Suzuki, T., and Verwaest, T. (2015). "Applicability of Smoothed Particle Hydrodynamics for estimation of sea wave impact on coastal structures." *Coastal Engineering*, Elsevier B.V., 96, 1–12, https://doi.org/10.1016/j.coastaleng.2014.11.001.

Antuono, M., Marrone, S., Colagrossi, A., and Bouscasse, B. (2015). "Energy balance in the δ-SPH scheme." *Computer Methods in Applied Mechanics and Engineering*, 289(May), 209–226, https://doi.org/10.1016/j.cma.2015.02.004.

Burnett, K., Wada, C., Endo, A., and Taniguchi, M. (2016). *Cost-Benefit Analysis of Disaster Mitigation Infrastructure: The Case of Seawalls in Otsuchi, Japan*. University of Hawaii Economic Research Organization, University of Hawaii at Manoa.

Cantelmo, C., and Cuomo, G. (2020). "Hydrodynamic loads on buildings in floods." *Journal of Hydraulic Research*, 59(1), 61–74, https://doi.org/10.1080/00221686.2020.1714759.

Cunningham, L. S., Rogers, B. D., and Pringgana, G. (2014). "Tsunami wave and structure interaction: an investigation with smoothed-particle hydrodynamics." *ICE Journal of Engineering and Computational Mechanics*, 167(3), 126–138, https://doi.org/10.1680/eacm.13.00028.

Dehnen, W., and Aly, H. (2012). "Improving convergence in smoothed particle hydrodynamics simulations without pairing instability." *Monthly Notices of the Royal Astronomical Society*, 425(2), 1068–1082, https://doi.org/10.1111/j.1365-2966.2012.21439.x.

Domínguez, J. M., Fourtakas, G., Altomare, C., Canelas, R. B., Tafuni, A., García-Feal, O., Martínez-Estévez, I., Mokos, A., Vacondio, R., Crespo, A. J. C., Rogers, B. D., Stansby, P. K., and Gómez-Gesteira, M. (2021). "DualSPHysics: from fluid dynamics to multiphysics problems." *Computational Particle Mechanics*, Springer International Publishing, (0123456789), https://doi.org/10.1007/s40571-021-00404-2.

Fourtakas, G., Dominguez, J. M., Vacondio, R., and Rogers, B. D. (2019). "Local uniform stencil (LUST) boundary condition for arbitrary 3-D boundaries in parallel smoothed particle hydrodynamics (SPH) models." *Computers and Fluids*, Elsevier Ltd, 190, 346–

361, https://doi.org/10.1016/j.compfluid.2019.06.009.

Fukui, N., Chida, Y., Zhang, Z., Yasuda, T., Ho, T.-C., Kennedy, A., and Mori, N. (2022). "Variations in Building-Resolving Simulations of Tsunami Inundation in a Coastal Urban Area." *Journal of Waterway, Port, Coastal, and Ocean Engineering*, 148(1), 1–14, https://doi.org/10.1061/(asce)ww.1943-5460.0000690.

Gomez-Gesteira, M., Rogers, B. D., Crespo, A. J. C., Dalrymple, R. A., Narayanaswamy, M., and Dominguez, J. M. (2012). "SPHysics – development of a free-surface fluid solver – Part 1: Theory and formulations." *Computers & Geosciences*, Elsevier, 48(1), 289–299, https://doi.org/10.1016/j.cageo.2012.02.029.

Goring, D. G. (1978). "Tsunamis - The Propagation of Long Wave onto A Shelf." REP Kh-R-38, W. M. Keck Laboratory of Hydraulic and Water Resources, California Institute of Technology, Pasadena, CA.

Ishii, H., Takabatake, T., Esteban, M., Stolle, J., and Shibayama, T. (2021). "Experimental and numerical investigation on tsunami run-up flow around coastal buildings." *Coastal Engineering Journal*, Taylor & Francis, 63(4), 485–503, https://doi.org/10.1080/21664250.2021.1949920.

Kihara, N., Arikawa, T., Asai, T., Hasebe, M., Ikeya, T., Inoue, S., Kaida, H., Matsutomi, H., Nakano, Y., Okuda, Y., Okuno, S., Ooie, T., Shigihara, Y., Shoji, G., Tateno, T., Tsurudome, C., and Watanabe, M. (2021). "A physical model of tsunami inundation and wave pressures for an idealized coastal industrial site." *Coastal Engineering*, Elsevier B.V., 169(July), 103970, https://doi.org/10.1016/j.coastaleng.2021.103970.

Kleefsman, K. M. T., Fekken, G., Veldman, A. E. P., Iwanowski, B., and Buchner, B. (2005). "A Volume-of-Fluid based simulation method for wave impact problems." *Journal of Computational Physics*, 206, 363–393.

Linton, D., Gupta, R., Cox, D., van de Lindt, J., Oshnack, M. E., and Clauson, M. (2013). "Evaluation of Tsunami Loads on Wood Frame Walls at Full Scale." *Journal of Structural Engineering*, 139(8), 1318–1325, https://doi.org/10.1061/(ASCE)ST.1943-541X.0000644.

Madsen, P. A., Fuhrman, D. R., and Schaffer, H. A. (2008). "On the solitary wave paradigm for tsunamis." *Journal of Geophysical Research*, 113, 1–22.

Moon, W. C., Lau, T. L., and Puay, H. T. (2020). "Experimental investigations of tsunami loading on internal wall of a building with various openings and wall configurations." *Coastal Engineering*, Elsevier B.V., 158(March), 103691, https://doi.org/10.1016/j.coastaleng.2020.103691.

Moris, J. P., Kennedy, A. B., and Westerink, J. J. (2021). "Tsunami wave run-up load reduction inside a building array." *Coastal Engineering*, Elsevier B.V., 169(April), 103910, https://doi.org/10.1016/j.coastaleng.2021.103910.

Pringgana, G., Cunningham, L. S., and Rogers, B. D. (2016). "Modelling of tsunami-induced bore and structure interaction." *Proceedings of the Institution of Civil Engineers: Engineering and Computational Mechanics*, 169(3), 109–125, https://doi.org/10.1680/jencm.15.00020.

Pringgana, G., Cunningham, L. S., and Rogers, B. D. (2021). "Influence of Orientation and Arrangement of Structures on Tsunami Impact Forces: Numerical Investigation with

Smoothed Particle Hydrodynamics." *Journal of Waterway, Port, Coastal, and Ocean Engineering*, 147(3), 04021006, https://doi.org/10.1061/(asce)ww.1943-5460.0000629.

Shafiei, S., Melville, B. W., and Shamseldin, A. Y. (2016). "Experimental investigation of tsunami bore impact force and pressure on a square prism." *Coastal Engineering*, 110, 1–16, https://doi.org/10.1016/j.coastaleng.2015.12.006.

Syamsidik, Tursina, Suppasri, A., Al'Ala, M., Luthfi, M., and Comfort, L. K. (2019). "Assessing the tsunami mitigation effectiveness of the planned Banda Aceh Outer Ring Road (BORR), Indonesia." *Natural Hazards and Earth System Sciences*, 19(1), 299–312, https://doi.org/10.5194/nhess-19-299-2019.

Thomas, S., Killian, J., and Bridges, K. (2015). "Influence of Macroroughness on Tsunami Loading of Coastal Structures." *Journal of Waterway, Port, Coastal and Ocean Engineering*, 141(1), 04014028, https://doi.org/10.1061/(ASCE)WW.1943-5460.0000268.

Tomiczek, T., Prasetyo, A., Mori, N., Yasuda, T., and Kennedy, A. (2016). "Physical modelling of tsunami onshore propagation, peak pressures, and shielding effects in an urban building array." *Coastal Engineering*, Elsevier B.V., 117, 97–112, https://doi.org/10.1016/j.coastaleng.2016.07.003.

Xu, Z., Melville, B., Whittaker, C., Nandasena, N. A. K., and Shamseldin, A. (2021). "Mitigation of tsunami bore impact on a vertical wall behind a barrier." *Coastal Engineering*, Elsevier B.V., 164(December), 103833, https://doi.org/10.1016/j.coastaleng.2020.103833.

Yeh, H., Liu, P. L. F., Briggs, M. J., and Synolakis, C. E. (1994). "Propagation and Amplification of Tsunamis at Coastal Boundaries." *Nature*, 372, 353–355.

Yeh, H., Sato, S., and Tajima, Y. (2013). "The 11 March 2011 East Japan Earthquake and Tsunami: Tsunami Effects on Coastal Infrastructure and Buildings." *Pure and Applied Geophysics*, 170(6–8), 1019–1031, https://doi.org/10.1007/s00024-012-0489-1.

Zhang, W. (2009). "An Experimental Study and A Three-Dimensional Numerical Wave Basin Model of Solitary Wave Impact on A Vertical Cylinder." *School of Civil and Construction Engineering*, Oregon State University.

Zhang, Z., Kennedy, A. B., and Moris, J. P. (2023). "Tsunami wave loading on a structural array behind a partial wall." Coastal Engineering, Elsevier B.V., 179(May 2022), 104244, https://doi.org/10.1016/j.coastaleng.2022.104244.

Table 1. Detail of numerical model cases.

| Number of cases | Name of cases | Condition | | Size of Obstacle | | | |
| | | | | Height | | Length | |
		Barrier	Remarks	(*D*)	(m)	(*D*)	(m)
C1	BM	-	Baseline Model	-	-	-	-
C2	SW1	Straight wall	-	*D*/4	0.15	16*D*	9.60
C3	SW2	Straight wall	-	*D*/2	0.30	16*D*	9.60
C4	VW1	V-walls	-	*D*/4	0.15	2*D*	4.80
C5	VW2	V-walls	-	*D*/4	0.15	3*D*	7.20
C6	VW3	V-walls	-	*D*/4	0.15	4*D*	9.60
C7	VW4	V-walls	-	*D*/2	0.30	2*D*	4.80
C8	VW5	V-walls	-	*D*/2	0.30	3*D*	7.20
C9	VW6	V-walls	-	*D*/2	0.30	4*D*	9.60
C10	VWR1	V-walls	S22 rotated	*D*/2	0.30	2*D*	4.80
C11	VWR2	V-walls	S22 rotated	*D*/2	0.30	3*D*	7.20
C12	VWR3	V-walls	S22 rotated	*D*/2	0.30	4*D*	7.20
C13	VWX	V-walls	S22 excluded	*D*/2	0.30	4*D*	7.20

Table 2. SPH modeling constants value and parameters in DualSPHysics version 5.0

Coef. of sound	:	20	Boundary type	:	Dynamic (DBC)
Coefh	:	1.5	Kernel type	:	Wendland
CFL number	:	0.2	Step algorithm	:	Symplectic
Verlet steps	:	40	Solitary wave	:	Boussinesq
Viscosity	:	0.01	ViscoTreatment	:	Artificial
DensityDT value	:	0.1	DensityDT	:	Fourtakas (full)

Table 3. Numerical simulation time and number of particles

Numerical models	Simulation runtime (second)	Number of particles (d_p = 0.025m)			
		Fixed boundary	Moving boundary	Fluid particles	Total particles
BM	104,650	2,491,586			13,932,695
SW1	109,163	2,502,758			13,943,867
SW2	106,287	2,507,546			13,948,655
VW3	108,118	2,501,194	436,689	11,004,420	13,942,303
VW6	108,957	2,504,578			13,945,687
VWR3	108,025	2,503,910			13,945,019
VWX	108,050	2,501,120			11,004,420

Table 4. Maximum impact force on structures.

		SPH Numerical Models – Maximum impact force (N)											
	Structure	Baseline model	Model with 0.15 m-high barrier				Model with 0.30 m-high barrier				Model with 0.30 m-high barrier		
											Rotated S22		No S22
		BM	SW1	VW1	VW2	VW3	SW2	VW4	VW5	VW6	VWR1	VWR2	VWR3	VWX
				(L=2D)	(L=3D)	(L=4D)		(L=2D)	(L=3D)	(L=4D)	(L=2D)	(L=3D)	(L=4D)	(L=4D)
[1]	[2]	[3]	[4]	[5]	[6]	[7]	[8]	[9]	[10]	[11]	[12]	[13]	[14]	[15]
First bore impact	S11	978	406	656	489	307	461	724	177	112	568	198	134	129
	S12	1216	484	589	419	317	414	816	246	154	546	247	183	140
	S13	961	516	669	462	346	211	694	269	166	798	238	143	209
	S14	1115	692	726	419	339	306	697	174	110	651	158	143	110
	S21	1092	543	353	192	210	384	167	1	0	171	0	0	0
	S22	1057	544	1708	1752	1555	791	1819	1810	1291	1197	1002	769	-
	S23	1239	577	481	206	109	281	103	9	0	104	0	0	0
	S31	195	143	204	194	336	56	233	415	587	267	336	565	560
	S32	303	266	454	611	649	80	477	628	509	862	1057	789	738
	S33	297	280	435	729	605	41	441	612	691	757	1256	878	455
	S34	183	183	216	210	305	61	324	443	615	236	339	557	658
Second bore impact	S11	1238	975	1004	1221	1386	445	1117	835	503	1283	912	550	530
	S12	1373	1067	1102	1040	982	705	1209	770	534	1357	798	495	523
	S13	1261	1071	1116	1013	917	528	1205	778	458	1186	765	524	468
	S14	1289	1045	1028	1241	1030	590	1210	817	574	1336	847	490	609
	S21	1992	958	1002	1237	1073	691	561	650	440	814	580	480	433
	S22	1497	1391	2110	1352	1561	710	1404	2262	1288	1154	995	874	-
	S23	1870	995	975	883	970	1011	753	423	478	905	594	347	447
	S31	1059	597	567	472	433	478	586	363	369	357	368	473	385
	S32	979	927	629	618	670	420	579	519	486	686	761	715	409
	S33	1136	792	640	694	590	313	588	558	438	700	742	630	401
	S34	1003	668	558	495	531	361	454	380	383	358	458	384	381

Table 5. The percentage of maximum impact force reduction on structures over BM

Bore impact	Row	Model with 0.15 m-high barrier				Model with 0.30 m-high barrier							
		SW1	VW1	VW2	VW3	SW2	VW4	VW5	VW6	VWR1	VWR2	VWR3	VWX
[1]	[2]	[3]	[4]	[5]	[6]	[7]	[8]	[9]	[10]	[11]	[12]	[13]	[14]
1st	1	51	38	58	69	67	31	80	87	40	80	86	86
	2	51	25	37	45	57	38	46	62	57	70	77	100
	3	11	-34	-78	-94	76	-51	-115	-146	-117	-205	-185	-147
2nd	1	19	18	13	16	56	8	38	60	0	36	60	59
	2	38	24	35	33	55	49	38	59	46	60	68	75
	3	29	43	45	47	62	47	56	60	50	44	47	62

Table 6. Total impulse on structures.

		SPH Numerical Models − Total Impulse (N.s)												
	Structure	Baseline model	Model with 0.15 m-high barrier				Model with 0.30 m-high barrier				Model with 0.30 m-high barrier			
											Rotated S22			No S22
		BM	SW1	VW1 $(L=2D)$	VW2 $(L=3D)$	VW3 $(L=4D)$	SW2	VW4 $(L=2D)$	VW5 $(L=3D)$	VW6 $(L=4D)$	VWR1 $(L=2D)$	VWR2 $(L=3D)$	VWR3 $(L=4D)$	VWX $(L=4D)$
[1]	[2]	[3]	[4]	[5]	[6]	[7]	[8]	[9]	[10]	[11]	[12]	[13]	[14]	[15]
First and second bore impact	S11	2997	1396	2325	1750	1433	589	2439	1462	741	2417	1493	749	745
	S12	3042	1514	2570	1904	1548	537	2693	1665	792	2582	1676	812	728
	S13	2909	1633	2530	1997	1526	533	2648	1682	722	2636	1666	788	757
	S14	2810	1413	2349	1715	1469	526	2472	1448	767	2557	1472	739	723
	S21	3595	1810	1331	1070	1206	667	1144	721	512	1274	735	499	432
	S22	3486	1949	4756	4223	3903	710	4345	3857	3134	4005	3623	2861	-
	S23	3537	1824	1439	1123	1159	732	1274	686	584	1289	786	428	488
	S31	1901	1023	1204	1196	1329	339	1225	1279	1332	1035	1073	1334	1296
	S32	2038	1221	2098	2103	2145	497	1884	1926	1763	2432	2594	2204	1234
	S33	1998	1196	2144	2202	1959	437	1950	1947	1617	2332	2527	2107	1111
	S34	1839	1006	1161	1185	1317	312	1176	1255	1307	1005	1075	1312	1363
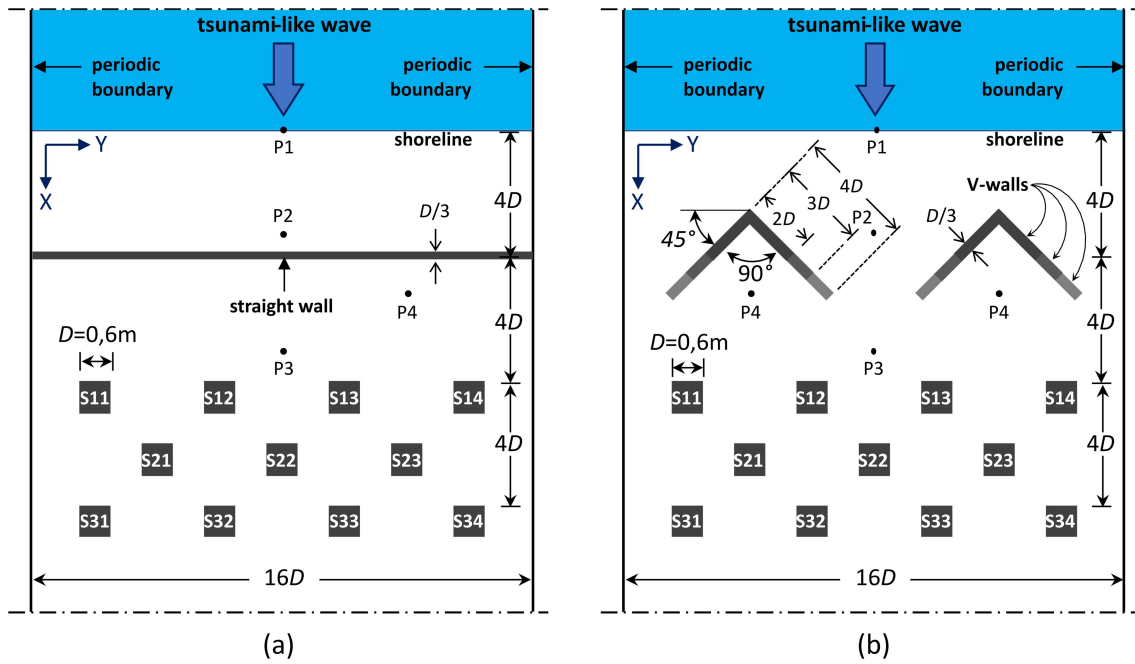
Figure 1
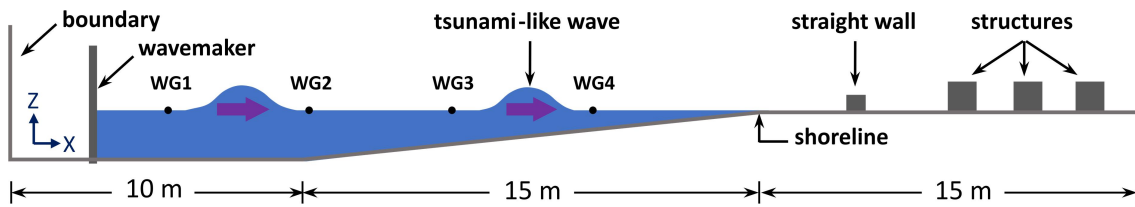
Figure 2
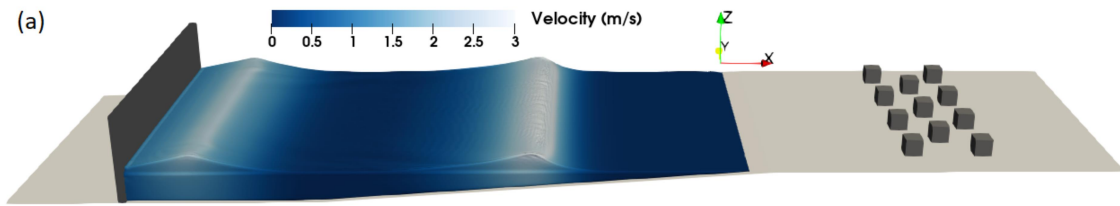
Figure 3a
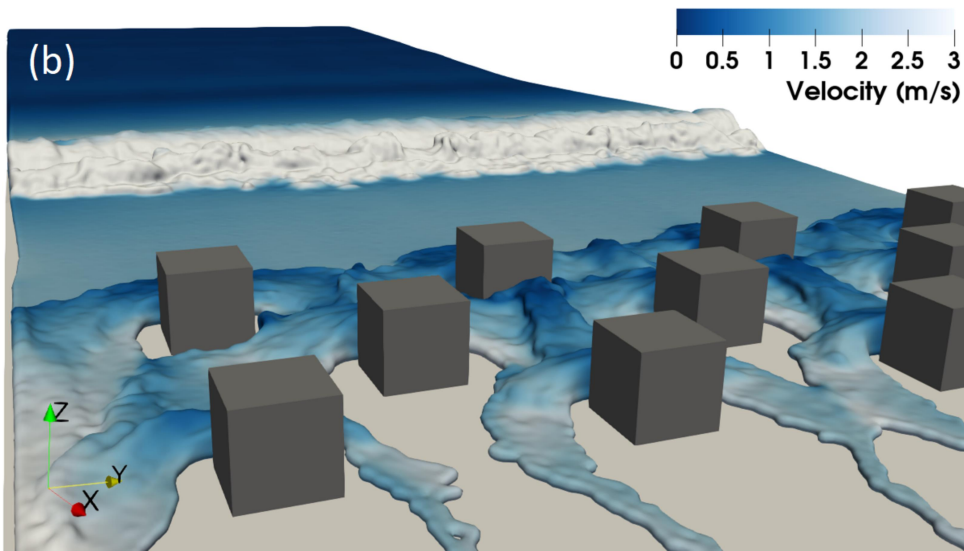
Figure 3b
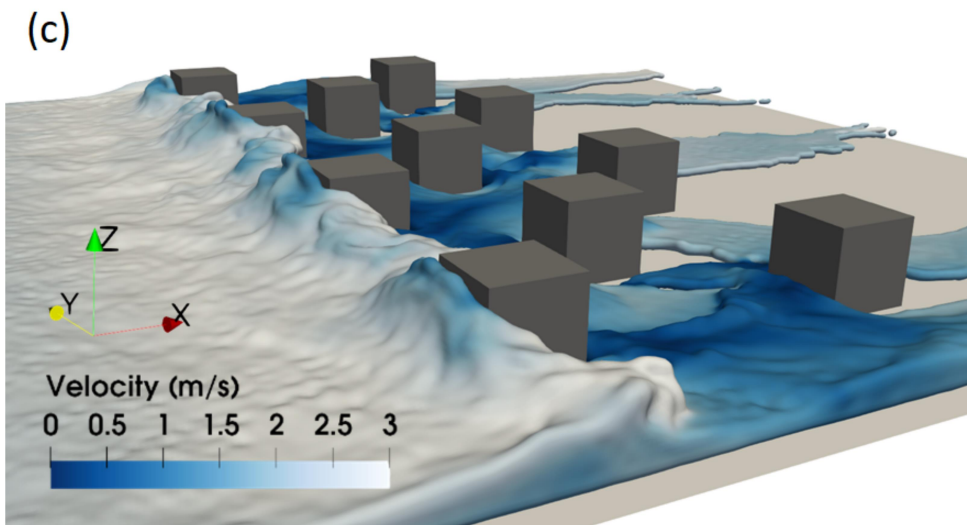
Figure 3c
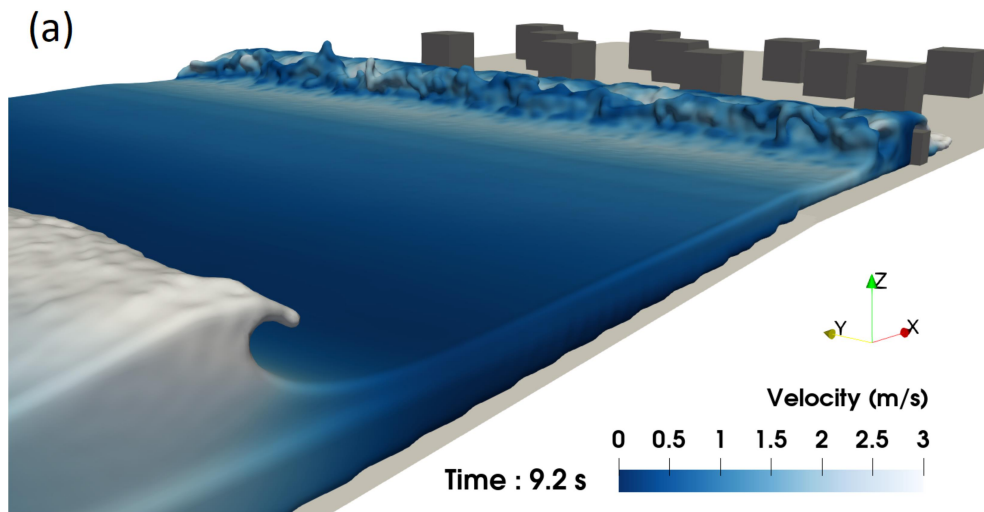
Figure 4a
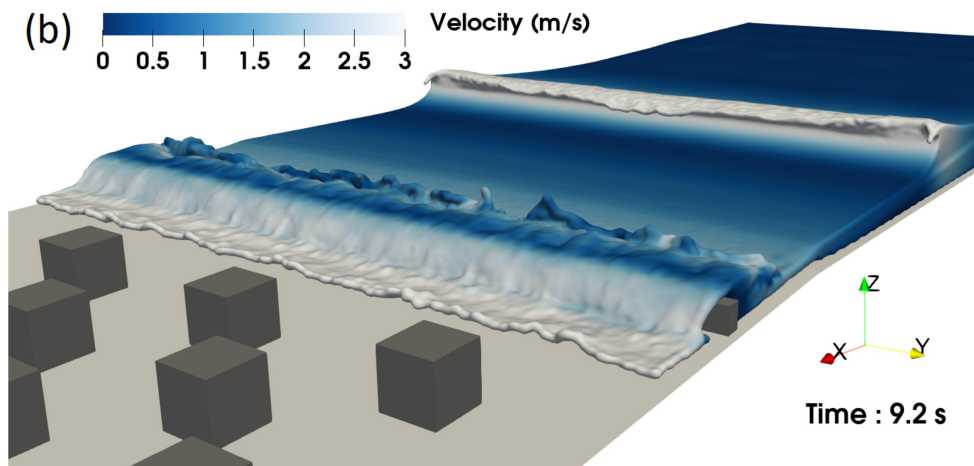
Figure 4b
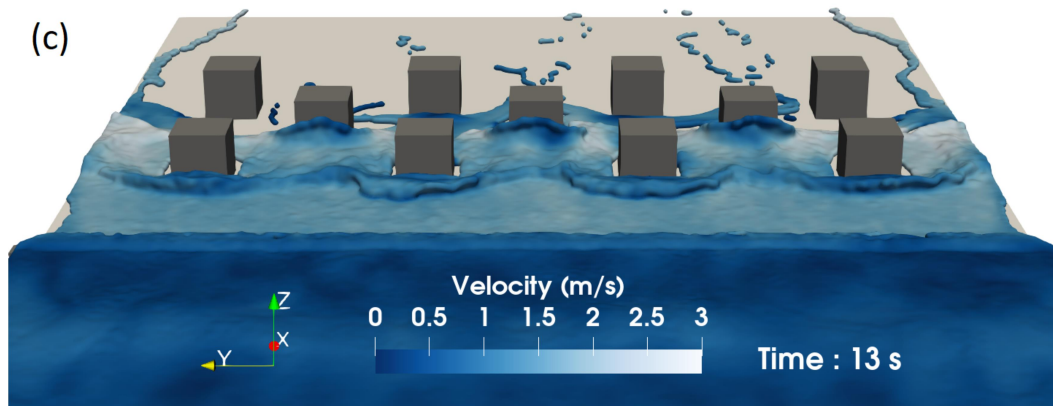
Figure 4c
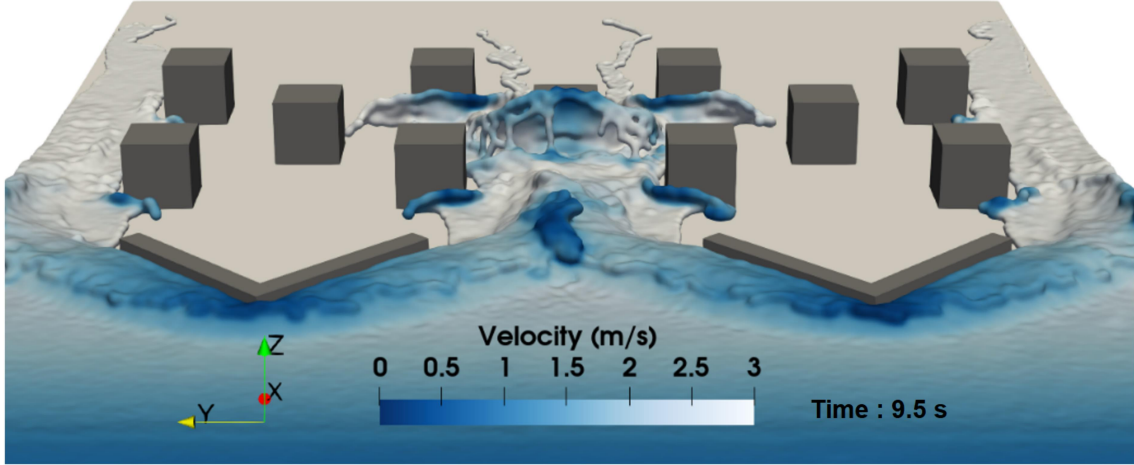
Figure 5
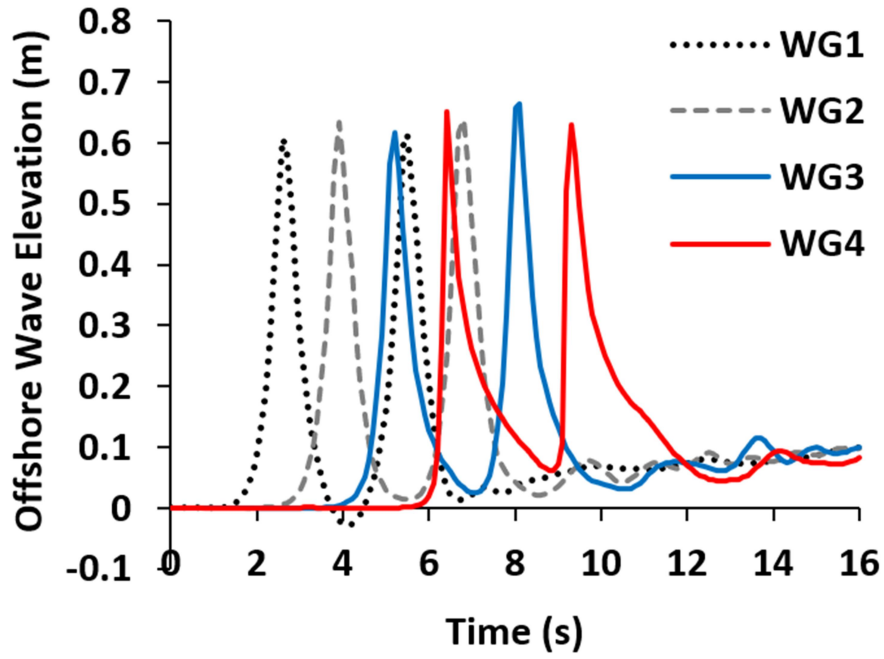
Figure 6a

Figure 6b

Figure 7a, 7b & 7c

34

Figure 8a, 8b & 8c

(a)

Time: 8.4 s

Velocity (m/s)

0   1   2   3   4

(b)

Figure 9a & 9b

(c)

Velocity (m/s)

0   1   2   3   4

Time: 11.4 s

Figure 9c

(d)
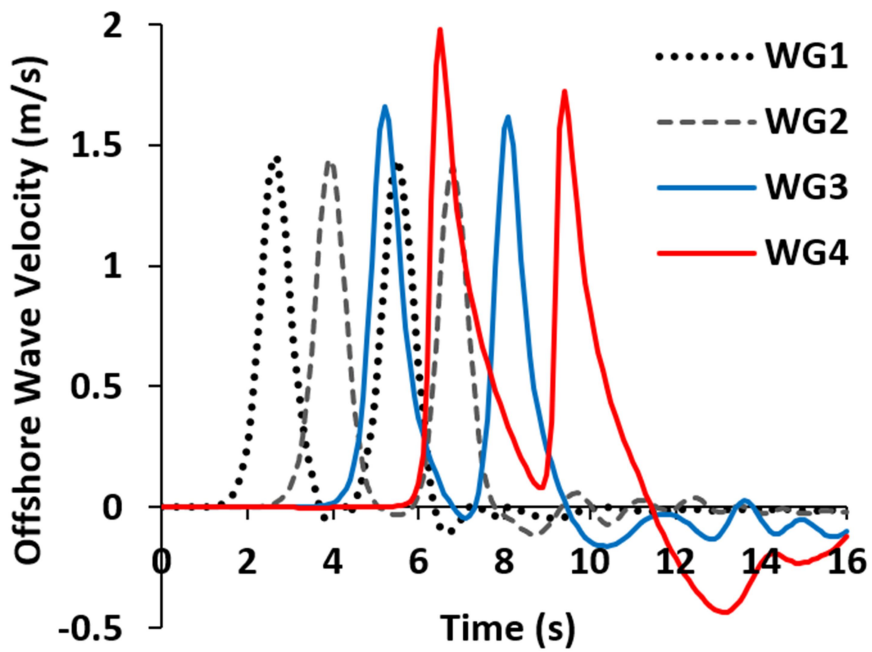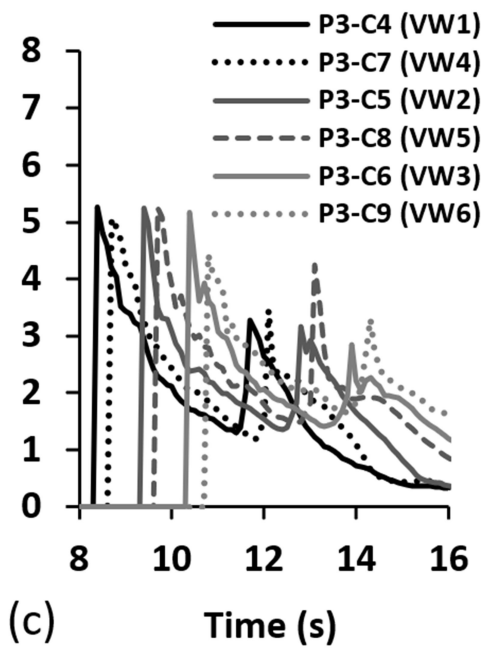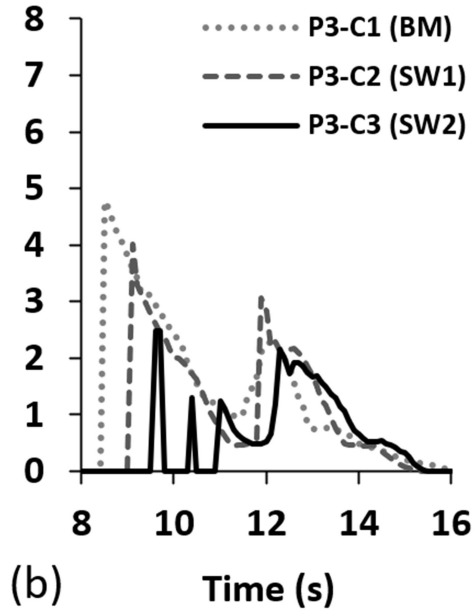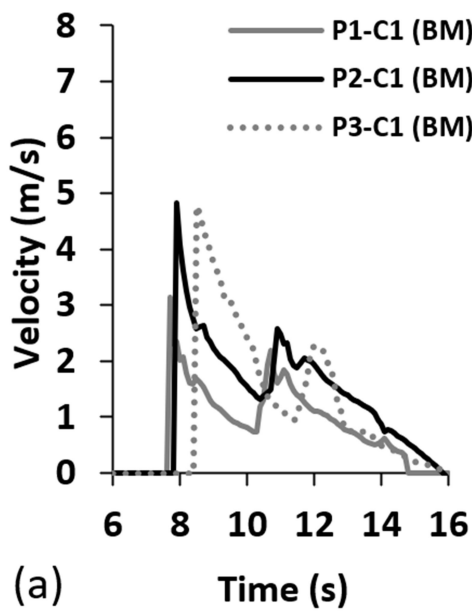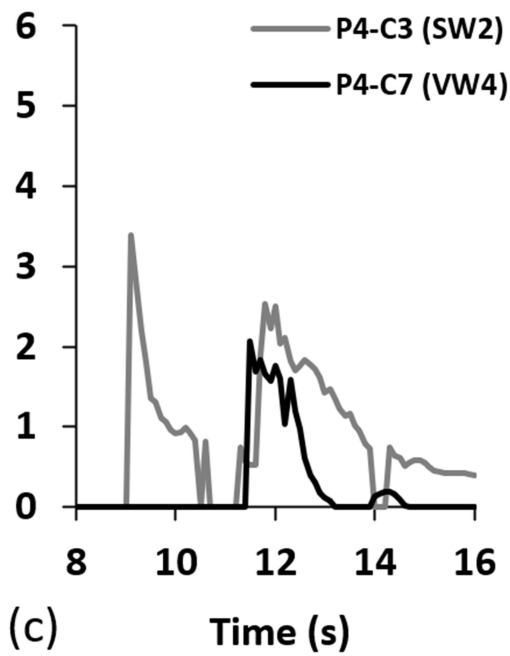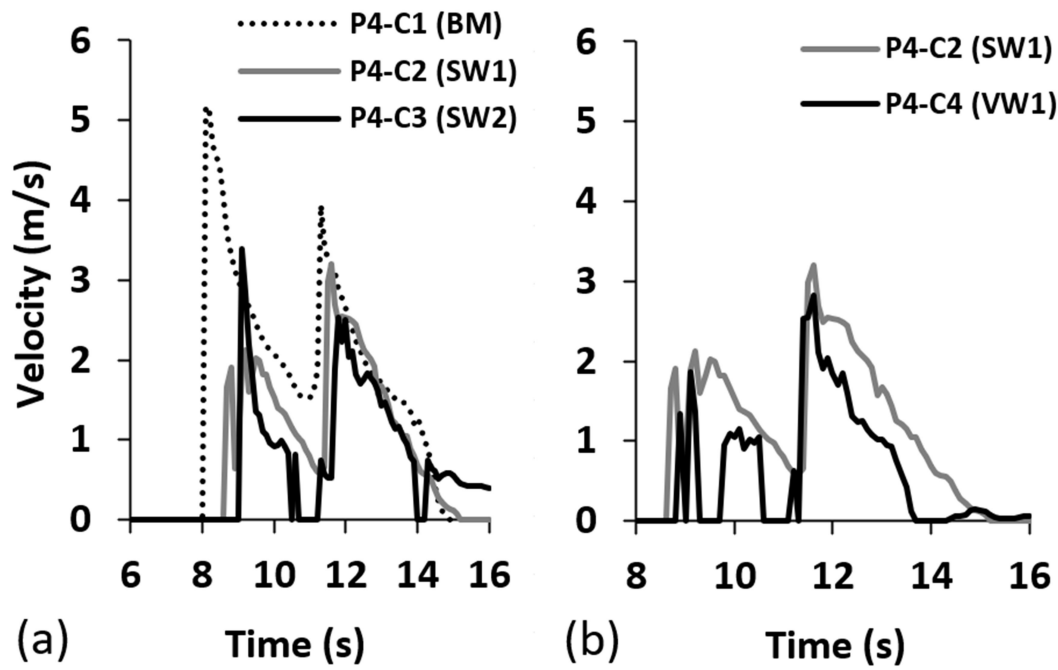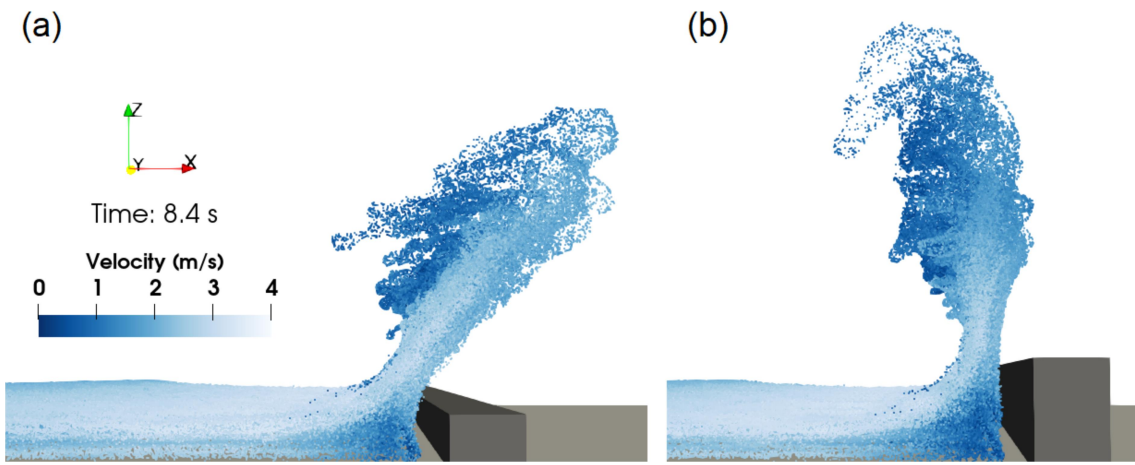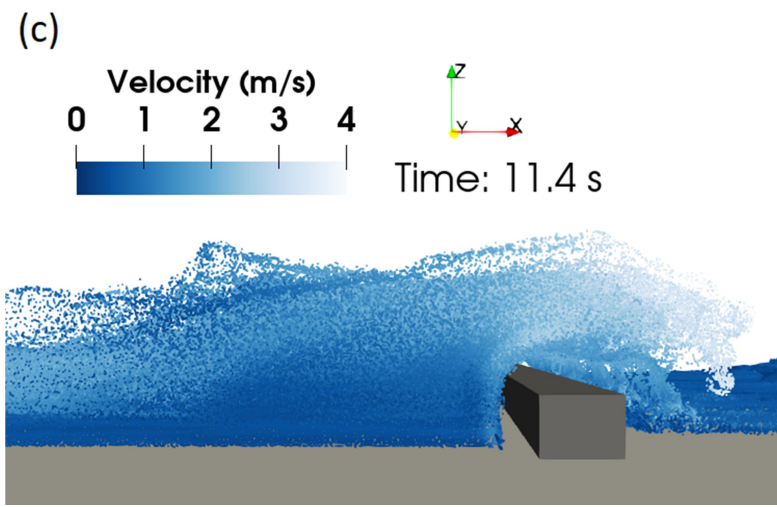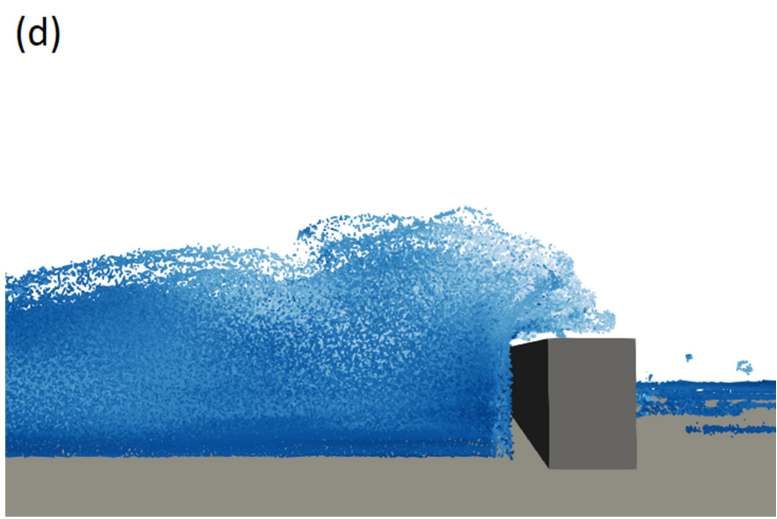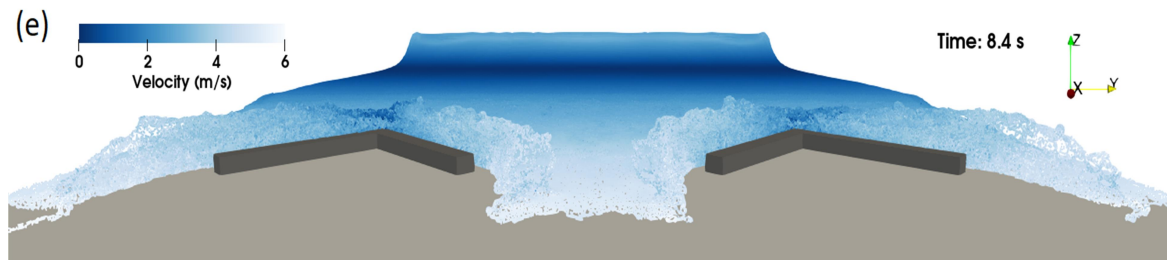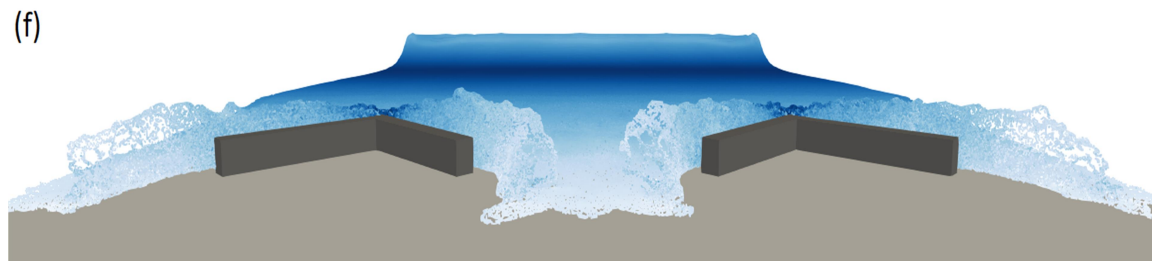
Figure 9d

Figure 9e

Figure 9f
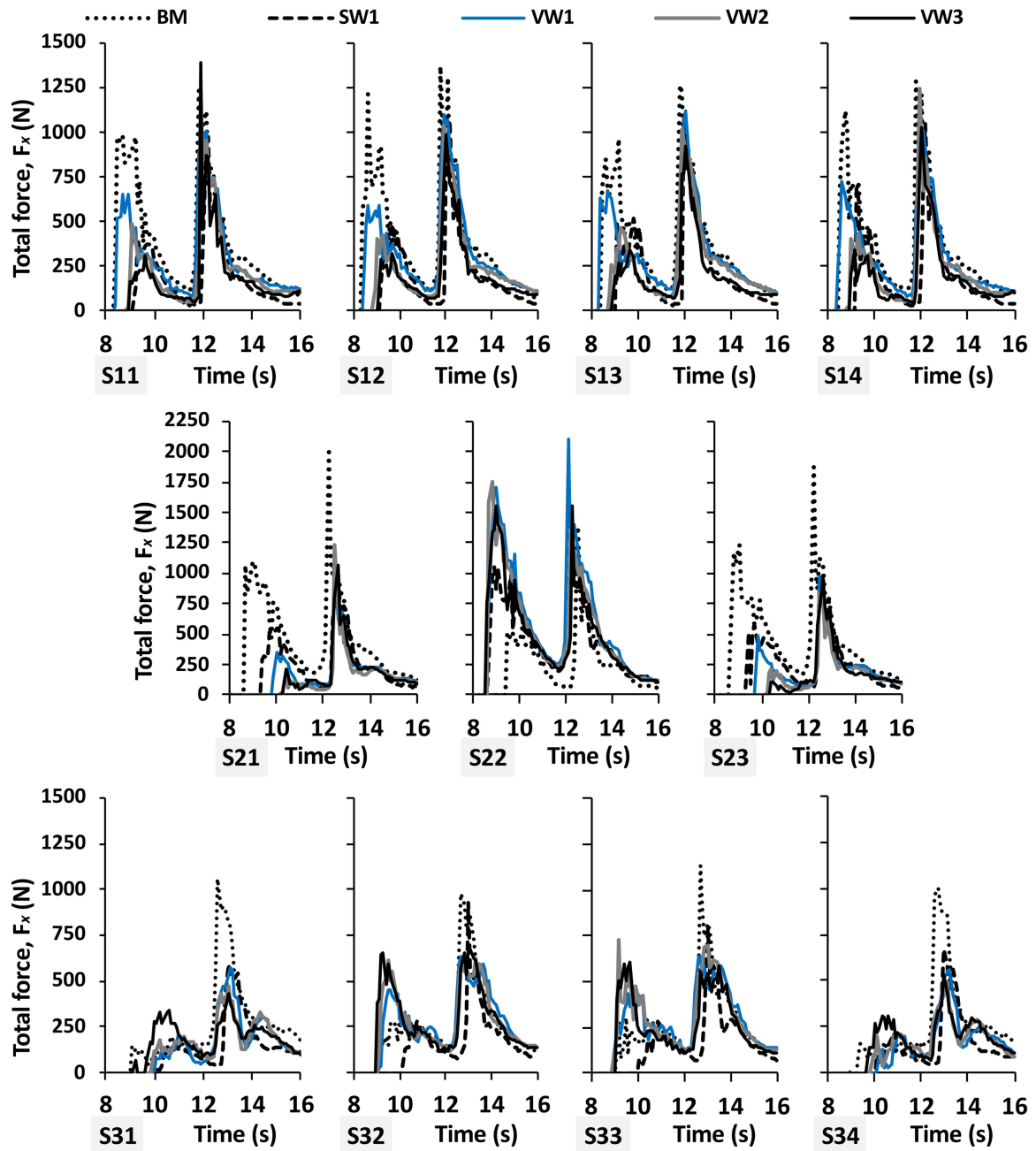
Figure 10
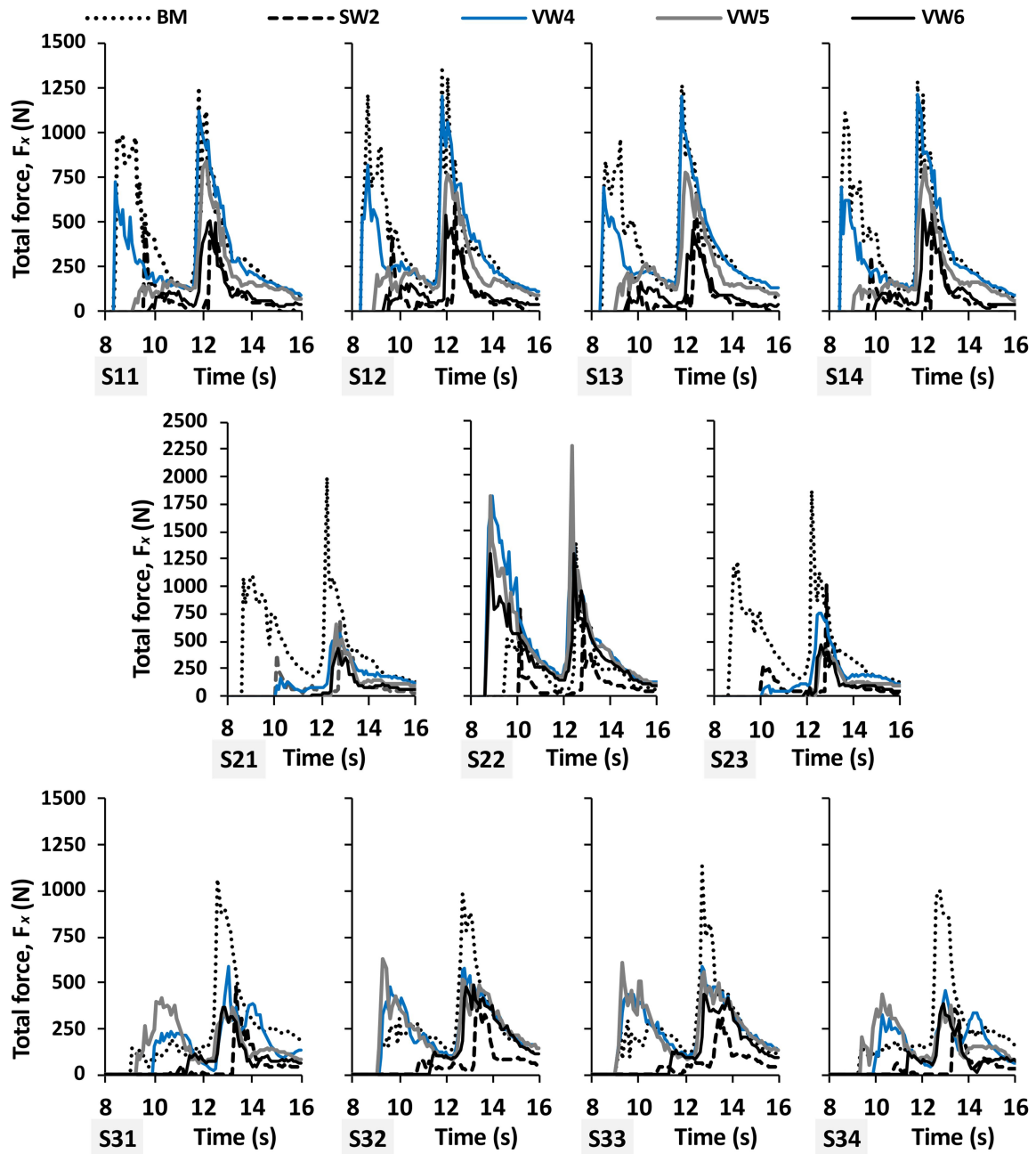
Figure 11
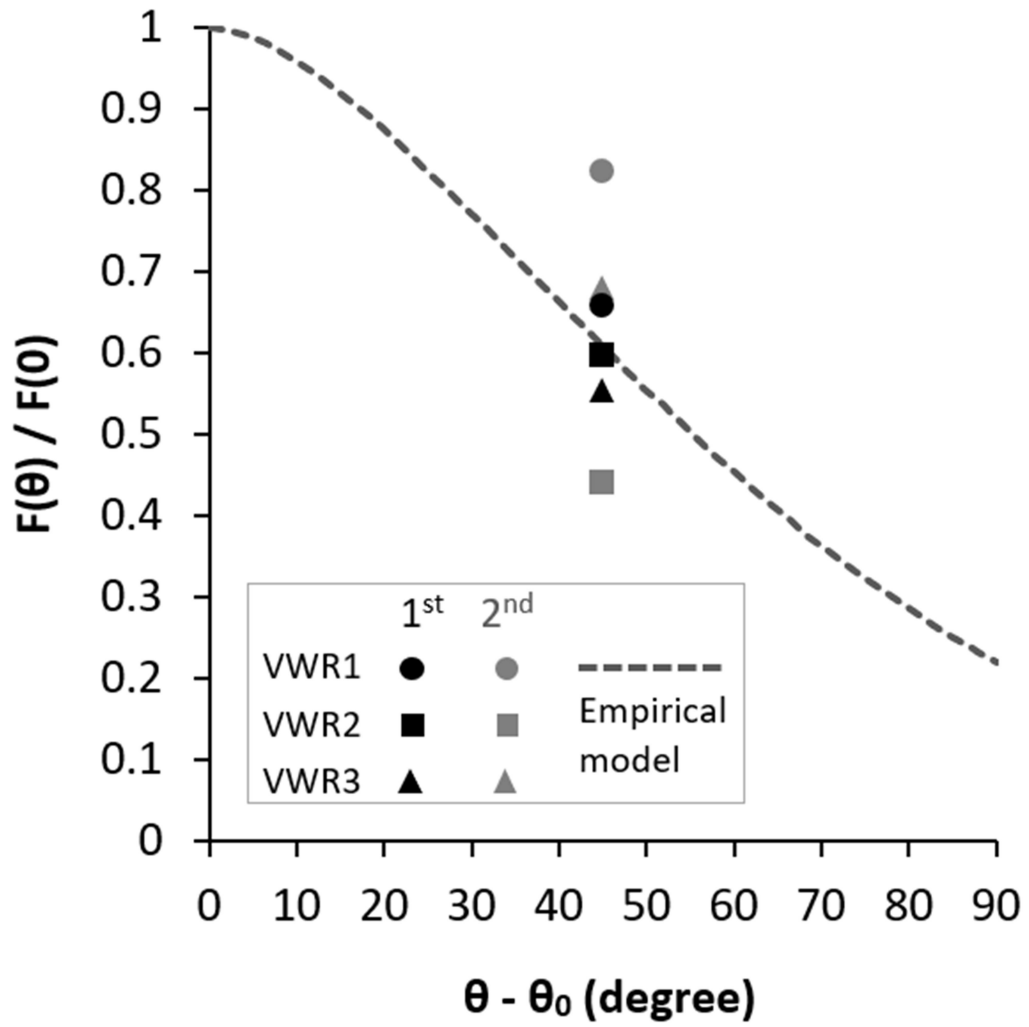
Figure 12

Figure 13a (left), 13b (right)

Figure 13c

Figure 14a (left), 14b (right)

Figure 14c
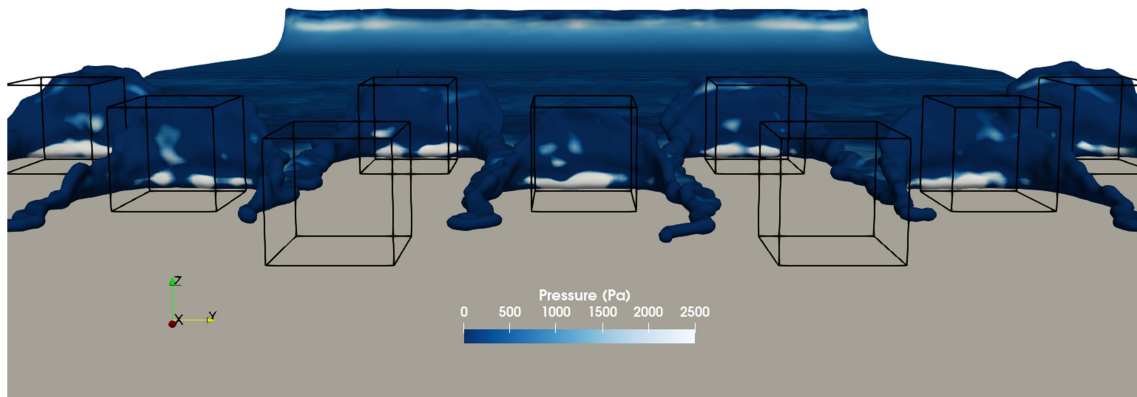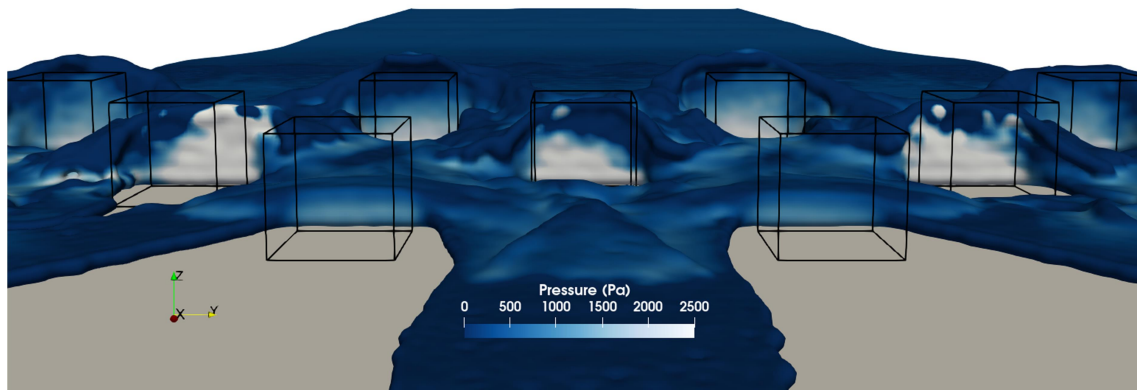
Figure 15a

Figure 15b
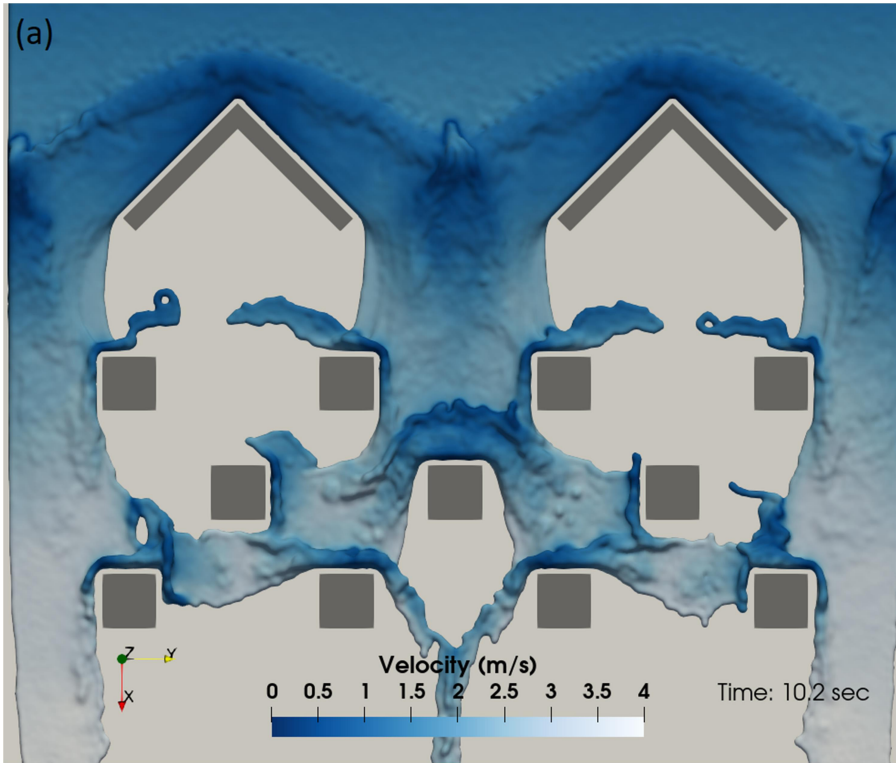
Figure A1a
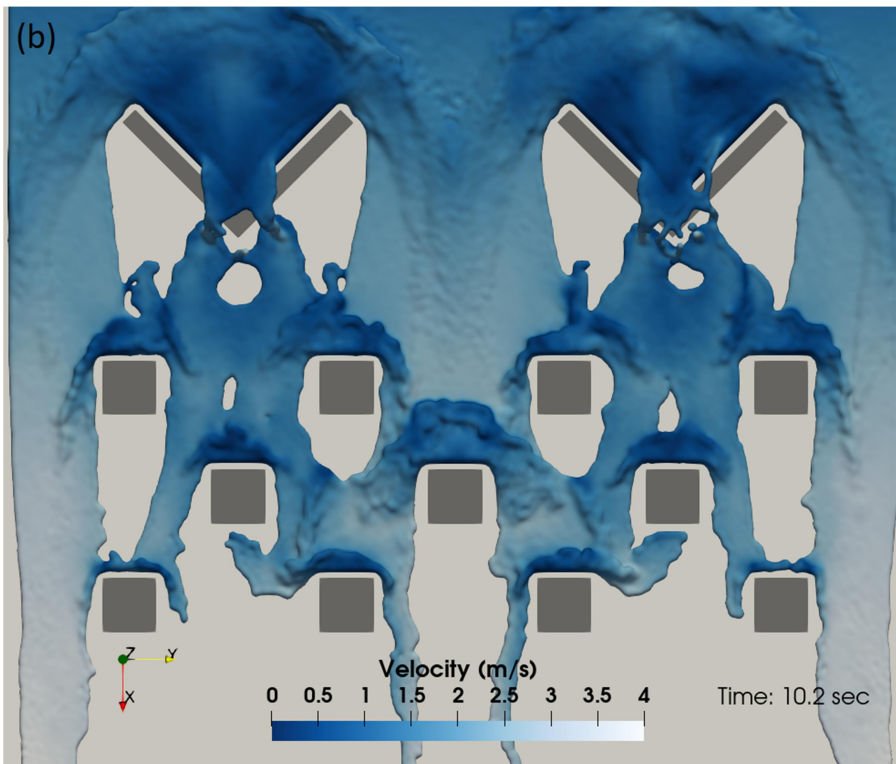
Figure A1b
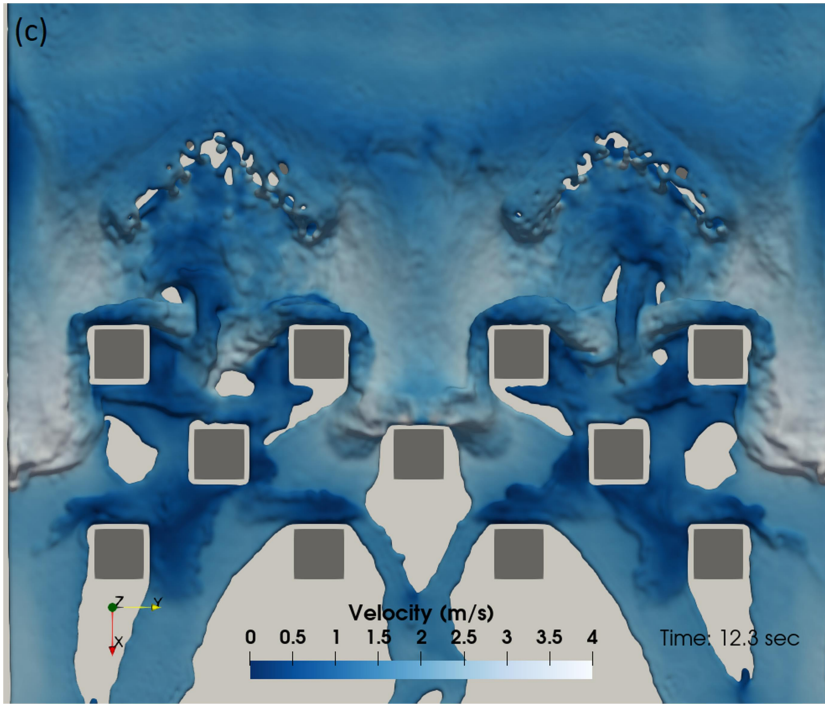
Figure A1c
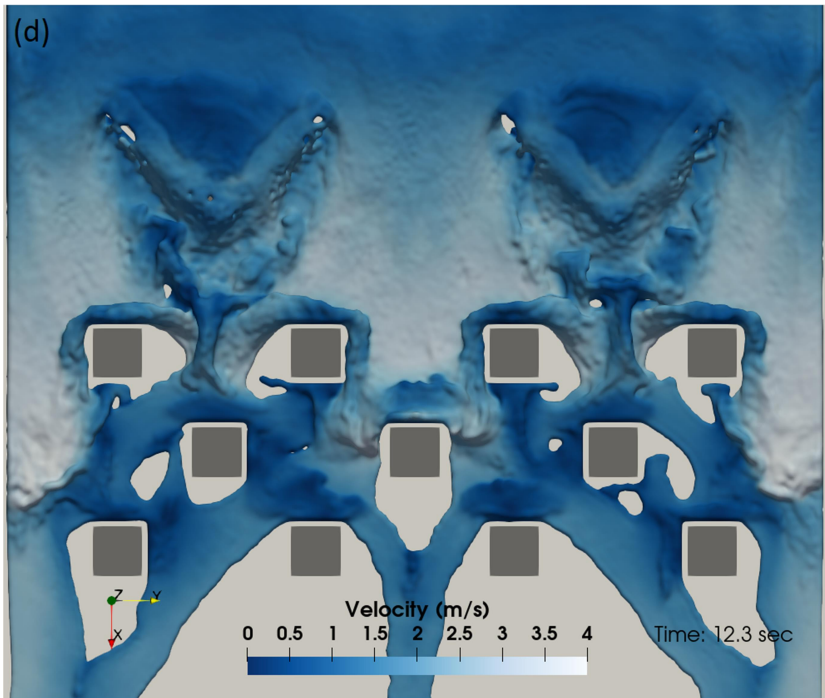
Figure A1d
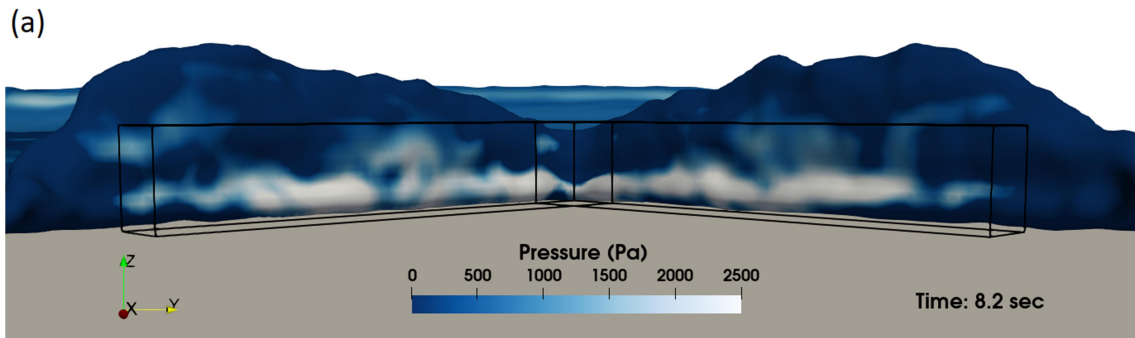
Figure A2a
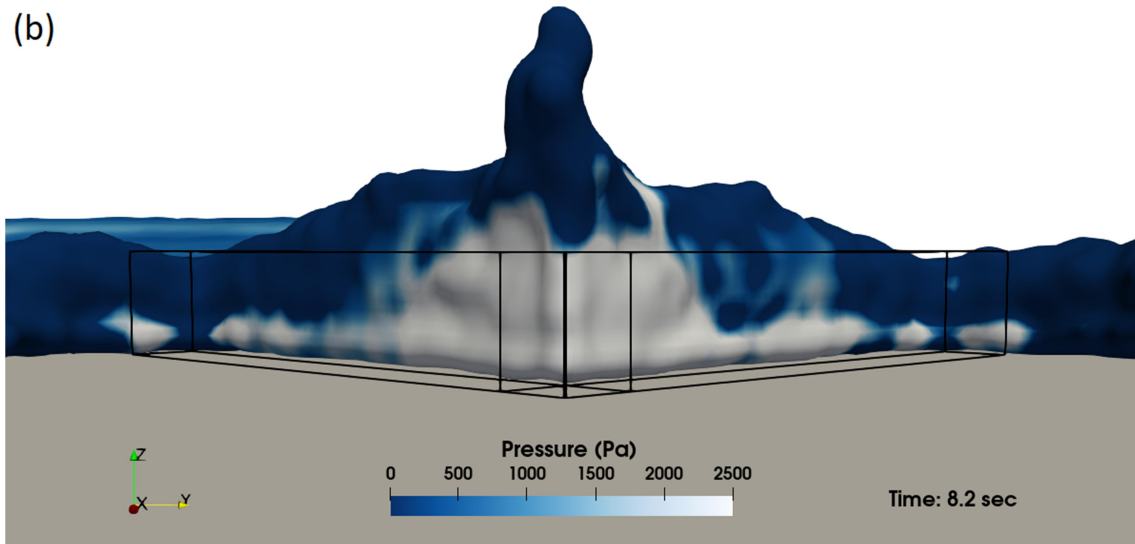
Figure A2b
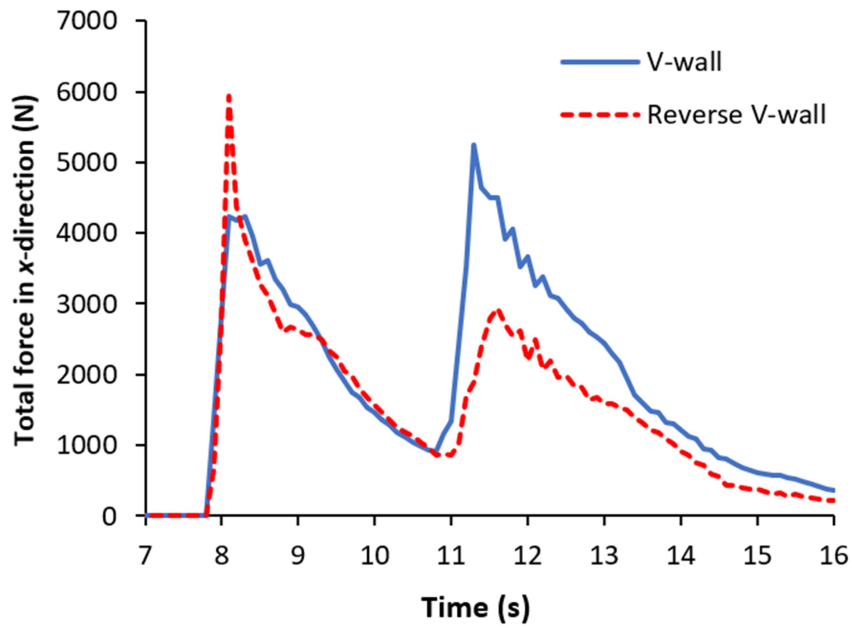
Figure A3

Figure A4

Figure A5